GLIA

Chronic demyelination of rabbit lesions is attributable to failed oligodendrocyte progenitor cell repopulation.

Journal:	*GLIA*
Manuscript ID	GLIA-00293-2022.R3
Wiley - Manuscript type:	Research Article
Date Submitted by the Author:	07-Dec-2022
Complete List of Authors:	Cooper, James; University at Buffalo, Polanco, Jessie; University at Buffalo, Neuroscience Saraswat, Darpan; University at Buffalo, Pharmacology & Toxicology Peirick, Jennifer; University at Buffalo, Laboratory Animal Facility Seidl, Anna; University at Buffalo, Pharmacology & Toxicology Li, Yi; University at Buffalo, Pharmacology & Toxicology Ma, Dan; Aston University, Aston Medical Research Institute Sim, Fraser; University at Buffalo, Pharmacology and Toxicology
Topics:	Oligodendrocytes, CNS myelin, Multiple sclerosis
Techniques:	Immunocytochemistry, In situ hybridization, Histological techniques
Key Words:	Remyelination, Models, Oligodendroglia

SCHOLARONE™
Manuscripts

Chronic demyelination of rabbit lesions is attributable to failed oligodendrocyte progenitor cell repopulation.

James J. M. Cooper, BS[1], Jessie J. Polanco, PhD[2], Darpan Saraswat, PhD[1], Jennifer Peirick, DVM[3], Anna Seidl[1], Yi Li[1], Dan Ma, PhD[4], Fraser J. Sim, PhD[1,2]

Department of Pharmacology and Toxicology[1], Neuroscience Program[2], Lab Animal Facilities[3], Jacobs School of Medicine and Biomedical Sciences, University at Buffalo, Buffalo, NY.

Translational Medicine Research Group[4], Aston Medical School, Aston University, Birmingham, United Kingdom.

Address correspondence to:

Fraser Sim, Ph.D.
Department of Pharmacology and Toxicology
Jacobs School of Medicine and Biomedical Sciences
University at Buffalo
955 Main Street
Buffalo, NY 14203
716-829-2151
fjsim@buffalo.edu

Topics: Oligodendrocyte, CNS myelin, Multiple sclerosis
Keywords: Remyelination, models

Main Points:
- Chronic demyelination in the rabbit CNS was associated with reduced OPC repopulation.
- Quiescent OPCs accumulated around the edge of rabbit lesions.
- OPC and oligodendrocyte repopulation was reduced in rabbit regardless of lesion volume.

Running title: Poor OPC Repopulation in Rabbit Demyelination
Abstract, 245; Introduction, 846; Discussion, 1787; Tables: 0, Figures: 9

Acknowledgements: This work was supported by the Department of Defense Congressionally Directed Medical Research Programs (W81XWH-21-1-0387), NINDS grant (R01NS104021), National Multiple Sclerosis Society (RG-1701-26750 and PP-1706-28080), the Kalec Multiple Sclerosis Foundation, and the Change MS Foundation. JJP received additional support from NIGMS (R25GM09545902), NCATS (UL1TR001412-S1), and New York State Department of Health (Empire State Stem Cell Fund) through the Stem Cells in Regenerative Medicine Fellowship (NYSTEM C30290GG). We acknowledge support provided by the Center for Computational Research at the University at Buffalo for use of the academic compute cluster for training the Keras-based convolution network. We also thank JA17 for is his support and motivation during this project.

Conflict of Interest: The authors declare no competing financial interests.

Abstract

The failure of remyelination in the human CNS contributes to axonal injury and disease progression in multiple sclerosis (MS). In contrast to regions of chronic demyelination in the human brain, remyelination in murine models is preceded by abundant oligodendrocyte progenitor cell (OPC) repopulation, such that OPC density within regions of demyelination far exceeds that of normal white matter. As such, we hypothesized that efficient OPC repopulation was a prerequisite of successful remyelination, and that increased lesion volume may contribute to the failure of OPC repopulation in human brain. In this study, we characterized the pattern of OPC activation and proliferation following induction of lysolecithin-induced chronic demyelination in adult rabbits. The density of OPCs never exceeded that of normal white matter and oligodendrocyte density did not recover even at 6 months post-injection. Rabbit OPC recruitment in large lesions was further characterized by chronic Sox2 expression in OPCs located in the lesion core and upregulation of quiescence-associated Prrx1 mRNA at the lesion border. Surprisingly, when small rabbit lesions of equivalent size to mouse were induced, they too exhibited reduced OPC repopulation. However, small lesions were distinct from large lesions as they displayed an almost complete lack of OPC proliferation following demyelination. These differences in the response to demyelination suggest that both volume dependent and species-specific mechanisms are critical in the regulation of OPC proliferation and lesion repopulation and suggest that alternate models will be necessary to fully understand the mechanisms that contribute to failed remyelination in MS.

INTRODUCTION

Disease-modifying therapies for the treatment of relapsing-remitting multiple sclerosis (MS) are effective at limiting neuroinflammation and reduce the rate of clinical relapses (McGinley et al., 2021). However, treatment options for progressive disability in MS and agents capable of enhancing myelin repair are limited. The stimulation of remyelination has been proposed to restore neurological function and prevent neurodegeneration in regions of chronic demyelination. Although spared oligodendrocytes (OLs) may contribute to remyelination in MS and in some experimental models (Yeung et al., 2019, Duncan et al., 2018, Bacmeister et al., 2020), when large numbers of adult OLs are destroyed remyelination relies on the generation of new OLs by oligodendrocyte progenitor cells (OPCs) (Hughes et al., 2013, Zawadzka et al., 2010). The cellular processes of remyelination can be broadly divided into recruitment and differentiation phases (Franklin and Ffrench-Constant, 2017). During the recruitment phase, OPCs upregulate markers of activation, enter the cell-cycle and migrate into the demyelinated lesion resulting in tissue repopulation. The expression of activation markers, such as Sox2, are then downregulated as OPCs differentiate into OLs (Zhao et al., 2015). The differentiation phase occurs when OPC exit the cell cycle and differentiate into myelin-forming oligodendrocytes (Franklin and Ffrench-Constant, 2017). Newly generated OLs engage and ensheath denuded axons and upregulate myelin proteins resulting in the production of a thin myelin sheath with shorter internodes that is capable of restoring saltatory conduction (Lubetzki et al., 2020).

While remyelination is a common feature of early relapsing-remitting MS, remyelination failure becomes more common with increasing disease duration and age (Franklin and Ffrench-Constant, 2017, Neumann et al., 2019). Remyelination failure is thought to be due to the malfunction of one or more stages of OL regeneration: namely OPC recruitment, differentiation, or myelin formation (Franklin and Ffrench-Constant, 2017). While quiescent OPCs are associated with chronic demyelination in MS (Wolswijk, 1998), the prevailing theory in the field has been that remyelination fails in MS due to a failure of differentiation. In response, a number of drug candidates aimed at boosting endogenous remyelination through the promotion of OPC differentiation have been developed and advanced to clinical trials after successful preclinical results, notably opicinumab (anti-Lingo1) (Mi et al., 2005), clemastine (Mei et al., 2014), and bexarotene (Huang et al., 2011). Unfortunately, while all were able to improve a functional test indicative of remyelination in the optic nerve, they have largely failed to significantly improve clinical outcomes or primary imaging endpoints in initial trials (Green et al., 2017, Mellion et al., 2017, Cadavid et al., 2019, Brown et al., 2021). The paradoxical success of differentiation-

promoting therapies in rodent models, but little success in clinical trials, suggests fundamental differences in the rate-limiting steps between remyelination in animal models and human MS.

A defining feature of human MS lesions is the dramatic increase in volume relative to murine models. Although highly variable in size, the median volume of an individual human MS lesions is around 100 mm^3 (Kohler et al., 2019), whereas typical mouse lesions are < 1 mm^3 (Jean et al., 2003, Rusielewicz et al., 2014). If the number of OLs required for successful remyelination scales linearly with lesion volume, this predicts a requirement for 100-fold more myelinating cells in MS. In the case of focal demyelination, OPCs are recruited from the surrounding white matter (Sim et al., 2002). As such, the available pool of progenitors will scale with lesion surface area which, assuming a roughly spherical lesion, increases at the square root of volume. Thus, to achieve a similar density of OPCs, a ten-fold increase in OPC generation (representing 3 or more cell divisions) and/or substantially improved migration must occur. In murine models of demyelination, the density of OPCs rapidly rises 2-3 fold above that of normal white matter shortly following lesion formation (Sim et al., 2002, Ulrich et al., 2008, Kucharova and Stallcup, 2015, Lin et al., 2006). In contrast, OPC density in MS lesions rarely exceed that of normal appearing white matter (NAWM) (Lucchinetti et al., 1999, Kuhlmann et al., 2008, Boyd et al., 2013, Moll et al., 2013, Tepavcevic et al., 2014). These observations are consistent with an inability to scale OPC recruitment as lesion size increases.

In this study, we sought to model larger volumes of demyelination which were characterized by chronic demyelination. We selected the rabbit lysolecithin model of demyelination as it was originally characterized as exhibiting chronic demyelination for at least 6 months (Blakemore, 1978, Waxman et al., 1979, Foster et al., 1980). We found that the density of OPCs never exceeded that observed in rabbit NAWM. OPC repopulation was associated with a protracted period of OPC activation and relatively poor OPC proliferation. In addition, we observed an upregulation of quiescence associated marker Prrx1 (Wang et al., 2018, Saraswat et al., 2021b) in OPCs found at the lesion border at earlier timepoints. We found that these alterations were not solely due to volume, as 10-fold smaller lesions also displayed reduced OPC density and reduced proliferation. However, small lesions were distinct in that they contained almost no proliferating OPCs. Together, these observations suggest that both volume-dependent and species-specific differences in the OPC response to demyelination contribute to the capacity of animal models to undergo spontaneous remyelination.

131 **MATERIALS AND METHODS**

132 *Animals and surgery*

133 All experiments were performed according to protocols approved by the University at Buffalo's
134 Institutional Animal Care and Use Committee. New Zealand White Rabbits were purchased as
135 needed (Female, average weight 2.96 ± 0.13 kg, and average age 15.79 ± 0.53 weeks) (Charles
136 Rivers Laboratories, Wilmington, MA). Induction anesthesia was accomplished via intramuscular
137 injection of ketamine (35 mg/kg) and xylazine (5 mg/kg) into epaxial muscles. After loss of
138 consciousness, supplemental heating began, and corneas were lubricated. The proximal 3 cm of
139 the tail was shaved to provide an optimal location for the pulse oximetry probe (far preferable to
140 use of ear or tongue). ECG leads and rectal temperature probe were placed. After pre-
141 oxygenation via face mask, rabbits were intubated in ventral recumbency with heads and necks
142 held in extension. A size 3.0 endotracheal tube was threaded over an 8-French urinary catheter.
143 After placement of the catheter through the glottis, the ET tube was advanced over the catheter
144 and into the trachea. Successful intubation was verified via immediate capnography. Upon
145 success, isoflurane was delivered via Bain Circuit (1-3%). An IV catheter was placed (marginal
146 ear vein), and the surgical site was shaved and prepped prior to moving the rabbit to the operating
147 room (OR). Pre-emptive, initial analgesics were administered (0.05 mg/kg buprenorphine,
148 subcutaneously (SC) and 1.5 mg/kg carprofen, SC).

149 Once moved onto the OR table, rabbits were immediately reconnected to isoflurane to
150 ensure a suitable anesthetic plane. Then, they were transiently disconnected from the Bain Circuit
151 to allow loose movement of the head into the stereotaxic frame (Kopf Model 902 Small Animal
152 Stereotaxic Instrument + Kopf Model 1240 Rabbit Adaptor + Rabbit Risers, Kopf Instruments,
153 Tujunga, CA). The endotracheal (ET) tube, was carefully moved to rest between the arms of the
154 Kopf Rabbit Adaptor. It was important that the ET tube was not advanced beyond 12 cm to avoid
155 bronchial obstruction. Once positioned, the capnograph and Bain Circuit were quickly
156 reconnected. At this time further careful positioning of the rabbit's head was possible via tooth
157 bar, zygoma clamps, nose clamp. General anesthesia could be maintained for the remainder of
158 the stereotaxic procedure with isoflurane. Spontaneous respirations were augmented by manual
159 intermittent positive pressure ventilations (IPPV). 0.1 mL bupivacaine (0.25%) or lidocaine (2%,
160 diluted 1:1 with 0.9% NaCl) was injected SC. A 7-8 cm incision was made alone the midline of
161 the scalp to expose both bregma (intersection of the sagittal and coronal sutures) and lambda
162 (intersection of the sagittal and lambdoid sutures). Both left and right arm Hamilton needles were
163 filled with distilled H_2O to prevent occlusion and ensure flow prior to lysolecithin loading. Placing
164 the needles point on either bregma or lambda, the dorsal-ventral (DV) relationship was adjusted

using the Kopf Rabbit Adaptor until bregma was 1.5 mm above lambda. The arms of the Kopf frame were adjusted to a 20° angle, and the needle points were placed on bregma. The anterior-posterior (AP), lateral-medial (LM), and DV of each arm was recorded. The following adjustments were made to these values: AP= +0.5 mm, LM= +7.7 mm, DV= -5.7 mm. Injection sites were confirmed previously via Evans Blue injection. Drill bits (Burrs for Micro Drill 19007-29, 2.9 mm, Foster City, CA) were sterilized via dry micro bead bench side sterilizer for 1 minute and cooled with room temp saline. In advance of drilling, topical articaine (4%) was dripped onto the skull and allowed to absorb and dry over drilling skull sites. Drill holes were made through the skull to the level of the meninges with constant saline stream to prevent parenchymal heat damage. A 30G needle was then used to puncture the meninges to allow for free passage of the Hamilton needle. 1% lysolecithin was then injected at a rate 0.1 µl/min, with 5-minute wait times between microliters to allow for diffusion. Once injection was completed, the needles were left in place for 20 additional minutes to allow for diffusion. Either 5 µL (large volume lesion) or 0.35 µL (small volume lesion) or lysolecithin was injected.

Post-operatively, buprenorphine was administered (0.05 mg/kg, SC) 4 hours after the initial dose, and carprofen (1.5 mg/kg, SC) was continued twice daily for a total of 4 consecutive days. Rabbits were monitored daily after surgery and assessed for: mentation, weight loss from baseline, appetite, water consumption, amount and character of feces, amount of urination, and presence of neurologic signs. Post-surgical weight loss peaked at 28 dpl, followed by a rapid recovery (data available upon request).

Tissue processing

Animals were sacrificed at 7, 14, 21, 56, or 180 days post-lesion (dpl) by transcardial perfusion of saline followed by 4% paraformaldehyde under deep anesthesia. Following decapitation, whole brain tissue was extracted and post-fixed for 30 minutes in 4% paraformaldehyde. For cryopreservation, the tissue was first left in 1x PBS overnight, then transferred into a 7.5% sucrose solution overnight, and finally 15% sucrose overnight. Cryoprotected tissue was then frozen in optimal cutting temperature medium (Tissue-Tek). Serial, 16 µm-thick coronal sections were cut using a Leica cryostat and stored in -80 °C freezer until processing.

To identify lesion location and volume, every 10th section was washed with 1x PBST (x3 by 5 min), stained with FluoroMyelin for 1 hour at room temperature (1:300, Thermo Fisher Scientific) and 4′,6-Diamidino-2-phenylindole dihydrochloride (DAPI) for 3 min (1:5000, Sigma Aldrich), and mounted in prolong gold (Thermo Fisher Scientific). Lesions were identified as regions with lesser FluoroMyelin signal and corresponding hypercellularity by DAPI, compared to

surrounding white matter. Cross-sectional lesion areas were calculated for both left and right hemisphere lesions using the NIH ImageJ software, and the largest cross-sectional area for each lesion was identified as the lesion center.

Estimation of lesion volume

Lesion volume was calculated from the measured cross-sectional areas determined by FluoroMyelin staining using Cavalieri's estimator of morphometric volume (Rosen and Harry, 1990):

$$V_c = d\left(\sum_{i=0}^{n}(y_i)\right) - (t)y_{MAX}$$

Where V_c is the Cavalieri's estimated volume, d is the distance between sections, y_i is the cross-sectional area of section i, t is the thickness of the sections, and y_{MAX} is the largest cross-sectional area of the lesion. Since every 10th section was stained, $d =$ 160 μm, and $t =$ 16 μm.

Immunohistochemistry (IHC)

Slides immediately adjacent to the lesion centers, identified by FluoroMyelin staining, were used for all immunohistochemical procedures. In general, sections were permeabilized for 1 hour with 1% Triton X-100 (Alfa Aesar) and 0.25% Tween 20 (Calbiochem). Sections were blocked for 1 hour with a solution containing 0.5% Triton X-100, 5% bovine serum albumin (BSA), and 5% normal donkey serum. For cytoplasmic antigens such as CC1, sections were permeabilized with a 0.1% saponin and 1% normal donkey serum for 15 minutes and blocked for 1 hour with a 5% donkey serum and 0.05% saponin. Primary antibodies utilized were goat anti-Olig2 (1:100, R&D Systems), mouse anti-CC1 (1:50, Millipore), mouse IgG2a anti-SOX2 (1:100, R&D Systems), mouse IgG1 anti-Ki67 (1:25, Fisher Scientific), rat IgG2a anti-MBP (1:300, Abcam Inc.), goat IgG Smi311 & Smi312 (1:1000, BioLegend), rabbit IgG anti-App (1:500, Thermo Fisher), rabbit IgG anti-Iba1 (1:300, Wako Chemicals), and mouse IgG1 anti-Gfap (1:400, Sigma-Aldrich). Alexa 488, 594, and 647-conjugated secondary antibodies (Invitrogen) were used at 1:500. Lesion areas were captured at 10X, 20X, and 60X magnification using an Olympus IX83 with IX3-SSU motorized stage and image tiles stitched via cellSens software. Images of immunostained sections were aligned with their corresponding FluoroMyelin stained section to accurately mark lesion boundaries, with exclusion of any portion of the lesion which extends into the gray matter. Cell counts were determined via a semi-automated, machine learning assisted, counting process

229 (code available upon request). The Keras based convolution network was trained on a set of
230 ~3250 CC1 positive and ~3250 CC1 negative pre-classified images (supervised learning).

231 *Fluorescence in situ hybridization*

232 Fluorescence in situ hybridization was performed with probes targeting Prrx1 (GenBank
233 accession #NM_011127.2) mRNA by using the RNAscope Fluorescent Multiplex Detection Kit
234 (Advanced Cell Diagnostics) according to the manufacturer instructions and as described
235 previously (Wang et al., 2018, Saraswat et al., 2021a). Fixed sections were baked at 60°C for 30
236 minutes, washed with ethanol, tissue pretreatment with proprietary buffers. Probes were then
237 hybridized and fluorescent conjugated. Sections were counterstained with DAPI to visualize
238 nuclei. Positive signals were identified as punctate dots present in nucleus and cytoplasm.

239 *Statistics*

240 All statistical testing was completed using GraphPad Prism Version 8.4.0. The control group for
241 all analyses of cell numbers and phenotypes was normal white matter (NWM) from uninjured
242 animals, or normal appearing white matter (NAWM) from a region distant from the lesion. Groups
243 comprised either time-points following injection of lysolecithin, regional analysis within the lesion,
244 or small vs large volume lesions. For all reporting, an experimental unit comprised a single lesion.
245 A minimum of 4 experimental units (lesions) per group was set *a priori*, along with a requirement
246 for at least three animals per group. Criteria for lesion inclusion were established *a priori*. Only
247 lesions located within internal capsule white matter were included in the analysis. No white matter
248 lesions regardless of size were excluded from the analysis. Rabbits were allocated to each group
249 in a randomized fashion based on availability from the vendor and surgical schedule.
250 Experimental units for large and small lesion animals are displayed in **Table 1**. Experimental units
251 for normal uninjured animals: 6 hemispheres, 3 animals. Total animals involved in the study, 38.
252 Manual cell count validations for all quantitative measures were performed in a blinded fashion.
253 Normality of data was tested in GraphPad using the D'Agostino-Pearson omnibus test. For
254 analysis of time-series data, one-way ANOVA with Tukey's post-hoc testing was performed. For
255 analysis of time-series and region/volume delimited data, two-way ANOVA with Sidak's post-hoc
256 testing was performed. Pairwise post-hoc testing was only performed if supported by ANOVA.
257 Only a portion of pairwise comparisons were highlighted, however full pairwise statistical
258 comparisons are available upon request.

259 *Data availability*

260 The data that supports the findings of this study are available upon reasonable request.

261 **RESULTS**

262 **Large lysolecithin-induced lesions in the rabbit persisted for at least 180 days.**

263 To test the hypothesis that supernumerary densities of OPCs are required for efficient
264 remyelination we sought to characterize OPC dynamics in a model of inefficient remyelination.
265 Lysolecithin-induced lesions in the sizable white matter tracts of the rabbit have been noted to
266 persist for at least 180 days (6 months) (Blakemore, 1978, Foster et al., 1980, Waxman et al.,
267 1979). To induce demyelination, we stereotactically injected lysolecithin into the periventricular
268 white matter of adult New Zealand White rabbits (bilateral injections of 1% lysolecithin, 5 µl) (**Fig.**
269 **1A**). We first examined lesion formation at 14 days post lesion (dpl). Overlay of a mouse coronal
270 section included for size reference. Lysolecithin induced focal demyelination at the site of injection
271 and resulted in a clearly demarcated region of hypercellularity that precisely matched the region
272 of myelin loss (**Fig. 1B**, white dashed line). The mean maximal cross-sectional area (MCA) and
273 volume were greatest at early time points and significantly declined with time (volume: 14 vs 21
274 dpl, Tukey's p = 0.032; MCA: 14 vs 56 dpl, Tukey's p = 0.013) (**Fig. 1C-D**). Large regions of
275 demyelination persisted in the rabbit even at 180 dpl. Volumetric analysis by serial section
276 reconstruction of the lesion indicated a comet-like appearance with a relatively spherical region
277 of demyelination corresponding to the site of injection and a tapered region extending in the
278 posterior-ventral direction (**Fig. 1E**).

279 **Insufficient OPC repopulation in the rabbit was associated with slow and incomplete OL**
280 **generation.**

281 We next sought to characterize the population dynamics of OPCs and OLs following
282 demyelination in the rabbit brain (**Fig 2**). We used Olig2 to label the entire oligodendrocyte lineage
283 and coexpression of CC1 and Olig2 to label post-mitotic OLs (**Fig. 2A**). Following demyelination,
284 Olig2$^+$ cell density was significantly reduced more than three-fold at 7 dpl (NWM vs 7 dpl, Tukey's
285 p < 0.0001) and never exceeded that of normal white matter (NWM) thereafter (**Fig. 2B**). The
286 density of OPCs/immature oligodendrocytes, defined as CC1$^-$Olig2$^+$ cells, significantly increased
287 between 7 and 14 dpl and remained stable at later time points (7 dpl vs 14 dpl; Tukey's p = 0.009)
288 (**Fig. 2C**). Following lysolecithin injection, the lesion was essentially devoid of OLs at 7 dpl (NWM
289 = 877.8 ± 62 vs 7 dpl = 79.9 ± 14 cells/mm^2) (**Fig. 2D**). By 56 dpl, OL density had partially
290 recovered and reached a plateau but remained significantly reduced at nearly half that of NWM
291 at 56 dpl (NWM = 877.8 ± 62 vs. 56 dpl = 453.9 ± 64.65 cells/mm^2, Tukey's p < 0.0017). The
292 proportion of CC1$^+$ OLs amongst the Olig2$^+$ population has been used to infer the rate of OL
293 differentiation. Intriguingly, while the proportion of OLs significantly increased with time until 21

294 dpl (7 dpl vs 21 dpl; Tukey's p = 0.009) (**Fig. 2E**), the proportion of OLs did not increase at later
295 time points suggesting that on-going OL generation may not continue after this initial period. The
296 percentage of CC1$^+$ OLs among total Olig2 remained low at 180 dpl indicating a chronic change
297 in oligodendrocyte lineage homeostasis (NWM = 66.3 ± 3.2% vs 180 dpl = 42.2 ± 9.1%). Together,
298 these data suggest that OPC repopulation in the rabbit lesions occurring following demyelination
299 is insufficient to generate sufficient OLs necessary to repair these lesions.

300 **OPC activation and proliferation were impaired following demyelination in the rabbit.**
301 Insufficient OPC recruitment in the rabbit may result from a failure of parenchymal OPCs to
302 respond appropriately to environmental signals associated with demyelination, and could result
303 from a disruption of OPC migration, activation, and/or proliferation. While we lacked the ability to
304 directly measure migration, we instead assessed OPC activation and proliferation. The
305 transcription factor Sox2 is upregulated in activated adult OPCs following demyelination and is
306 necessary for OPC recruitment and successful remyelination (Zhao et al., 2015). As expected, in
307 normal rabbit white matter the majority of Olig2$^+$ cells were Sox2$^-$ and Ki67$^-$ (**Fig. 3A**). Following
308 demyelination, recruited OPCs progressively upregulated Sox2, such that the majority of Olig2$^+$
309 cells in the lesion area coexpressed Sox2 by 14 dpl (NWM = 3.2 ± 2%, 14 dpl = 51.4 ± 3%) (**Fig.
310 3B**). Overall, the density of Sox2$^+$Olig2$^+$ OPC peaked at 14 dpl (NWM vs 14 dpl, 14 dpl vs 180
311 dpl, Tukey's $p < 0.0001$ and $p < 0.0001$, respectively), and returned to control levels by 180 dpl
312 (NWM vs 180 dpl, Tukey's $p > 0.05$) (**Fig. 3B-E**). The pattern of Sox2$^+$ expression among OL
313 lineage cells largely corresponded with their proliferative capacity defined by Ki67 expression.
314 The proportion of Ki67$^+$ cells among the Olig2$^+$ population peaked at 14 dpl and returned to
315 baseline by 180 dpl (NWM vs 14 dpl, 14 dpl vs 180 dpl, Tukey's p = 0.004 and p = 0.02,
316 respectively) (**Fig. 3B-D, F**). Interestingly, the proportion of dividing Sox2$^+$Olig2$^+$ remained
317 elevated until 56 dpl but never exceeded 30% (NWM vs 56 dpl, Tukey's p = 0.025) (**Fig. 3G**).
318 Together, this indicates a protracted period of OPC activation, whereby OPC proliferation fails to
319 keep pace, and one that ultimately fails to result in supernumerary OPC repopulation.

320 **Microglial/macrophage response correlates with the pattern of OPC repopulation**
321 Next, we examined the microglial and astrocyte response following demyelination to determine
322 whether the failure to recruit supernumerary OPCs could be attributed to the pattern of the innate
323 immune response. In this regard, we noted substantial upregulation of Sox2 among Olig2
324 negative cells following demyelination (**Fig. 3B-D**). We confirmed that these Sox2$^+$ cells were
325 largely reactive Gfap$^+$ astrocytes that were concentrated within the center of the demyelinated
326 lesion (**Fig. 3H**). A substantial number of Sox2$^+$Olig2$^-$ cells were observed within the lesion at all

time points, with statistically greatest numbers at 56 dpl followed by a reduction at 180 dpl (NWM vs 56 dpl, 56 dpl vs 180 dpl, Tukey's $p = 0.045$ and $p = 0.018$, respectively) (**Fig. 3I**).

At 7 dpl, both microglial (Iba1) and astrocyte (Gfap) markers were upregulated throughout the demyelinated lesion with a relatively homogenous pattern throughout the lesion area (**Fig. 4A**). At higher magnification, Iba1$^+$ microglia largely adopted an ameboid morphology while astrocytes were hypertrophic and reactive in appearance (**Fig. 4A**, insets). At later timepoints both microglia/macrophage and astrocyte signals were more concentrated toward the lesion center (**Fig. 4B-D**). While Gfap immunoreactivity remained elevated through 180 days, Iba1 was more transient with a peak between 7-14 days. Consistent with this qualitative assessment, Iba1 mean florescent intensity (MFI) peaked at 7 and 14 days and was significantly elevated relative to normal appearing white matter (**Fig. 4E**) (NAWM; defined as matched uninjured corpus callosum from the same cohort of animals, n=29). Iba1 was elevated relative to NAWM at early time points up to and including 56 dpl (NAWM vs 56 dpl, Tukey's $p = 0.006$). However, Iba1 staining was reduced at 180 dpl (7 dpl vs 180 dpl, Tukey's $p < 0.0001$) (**Fig. 4E**). In contrast, the astrocytic response defined by Gfap area remained significantly elevated throughout the experimental time course, with significant Gfap upregulation vs. NAWM still apparent at 180 dpl (NAWM vs 180 dpl, Tukey's $p = 0.02$) (**Fig. 4F**). Gfap upregulation was stable as no significant pairwise differences were observed between 7 dpl and any later timepoint (Tukey's $p > 0.05$). Consistent with these observations, the total density of DAPI$^+$ nuclei in the lesion area peaked at 14 dpl and declined thereafter. DAPI$^+$ density was significantly decreased 56 vs. 14 dpl (Tukey's 14 vs 56 dpl, $p = 0.04$) (**Fig. 4G**). Together, these results suggest that astroglial and microglial responses are distinct from one another and, intriguingly, that the overall microglial rather than the astroglial response corresponded to the pattern of OPC activation and proliferation.

Interestingly, in the center of the lesion ameboid microglia/macrophages commonly formed vesicular structures which were observed at early 14 dpl (**Fig. 5A**), and later 56 dpl timepoints (**Fig. 5B**). These structures overwhelmingly represent myelin ladened microglia/macrophages, which were also present at 56 dpl, albeit at lower number (**Fig. 5C-E**). Additionally, while almost all of these vesicular Iba1$^+$ structures were ladened with myelin at 14 dpl, there were a significant portion at 56 dpl which did not demonstrate immunoreactivity to myelin debris or neurofilament (**Fig. 5D-E**). As myelin debris impairs remyelination (Kotter et al., 2006), these data suggest that inefficient myelin clearance in the lesion core may influence repair in the rabbit.

Large rabbit lesions display regional differences in cellularity, demyelination, and axonal loss.

Toxin-induced demyelination in mouse models is characterized by a region of hypercellularity which corresponds to the extent of myelin degeneration. We compared the extent of myelin loss defined by FluoroMyelin (FM) with the relative density of DAPI$^+$ nuclei between 7 and 180 dpl (**Fig. 6**). The region of demyelination, defined by loss of FM staining, was hypercellular at 7 dpl (**Fig. 6A**) and remained so thereafter. However, surrounding the region of demyelination (**Fig. 6A,** white dashed line), we also observed a region of mild hypercellularity compared to that of more distant white matter (**Fig. 6A'**, blue dashed line). We termed this region perilesion white matter (PLWM) and confirmed via quantitative analysis that the cell density was significantly elevated compared to distant NAWM (Tukey's p = 0.0002) (**Fig. 6B**). We next examined the relative area of the demyelinating lesion and the associated PLWM with respect to time. Interestingly, while the area of PLWM was smaller than the demyelinated lesion at earlier timepoints, the PLWM area exceeded that of the lesion by 56 dpl and further expanded at 180 dpl (**Fig. 6C**). To investigate the potential cellular identity of cells within the PLWM, we quantified the intensity of microglial and astrocytic staining in the PLWM compared to distant NAWM. At 21 dpl, the PLWM exhibited significantly increased staining for both Iba1 and Gfap consistent with an increased number of both microglia/macrophages and astrocytes (**Supplemental Fig. 1**).

Next, we confirmed demyelination using myelin basic protein (Mbp) immunofluorescence that corresponded with the loss of FM staining. Compared to myelin fiber staining in NAWM (**Fig. 6D**), abundant Mbp$^+$ myelin debris was observed at 7 dpl (**Fig. 6F/6F'**). The amount of myelin debris was substantially reduced by 21 dpl. By 56 dpl, there was a partial recovery of Mbp immunoreactivity within the lesion, but this was clearly distinct from NAWM (**Fig. 6F, 56 dpl**). Within the PLWM, we did not observe myelin debris at earlier timepoints (7 and 21 dpl), and the pattern and intensity of staining closely resembled NAWM. However, at 56 and 180 dpl we observed subtle changes in the PLWM with reduced Mbp intensity and uneven staining.

Consistent with primary demyelination, neurofilament (NF)-labelled axons were observed at all time points in the lesion (**Fig. 6G, Supplemental Fig. 2**). The center of the large rabbit lesion displayed a small area of localized axonal loss (9-13% of total lesion area) that remained stable in size thereafter (**Supplemental Fig. 2G**). Consistent with the loss of axons in the lesion center, we observed accumulation of App immunoreactivity specifically at 7 dpl which disappeared at later time points (**Fig. 6G'**).

391 **Rabbit lesions exhibit region specific gradients of OPC activation and OL differentiation.**
392 The distribution and transcriptional profile of OPCs and OLs have been shown to be dependent
393 on their location within the lesion (e.g., core & periphery) (Boyd et al., 2013, Absinta et al., 2021).
394 The larger rabbit lesions allowed for correlation between OPC density and the local gliotic
395 response in specific intra-lesional regions. The lesion edge was defined as the 75 μm wide band
396 extending into the region of demyelination from the lesion border, the remainder of the lesion will
397 be hereafter referred to as lesion core. We examined OPC density and differentiation in each
398 region (**Fig. 7A-E**). The lesion core and lesion edge displayed similar amounts of hypercellularity,
399 with lesser amount of cellularity in the PLWM (**Fig. 7A**). We observed a reduction in OL density
400 ($CC1^+Olig2^+$) that corresponded to location within the lesion, such that OL density was lowest in
401 the lesion core and was significantly greater in the PLWM (Two-way ANOVA, region; $F(2,56)$
402 $=10.72$, $p = 0.0001$) (**Fig. 7B, 7F**). Consistent with a failure to repair regardless of region, the
403 density of OLs in the PLWM remained significantly depressed relative to normal white matter
404 (unpaired t test, two-tailed, NWM = 877.8 ± 62 vs PLWM at 180 dpl = 591.7 ± 110, $p = 0.048$).
405 Rabbit lysolecithin lesions exhibited the greatest $Olig2^+CC1^-$ defined OPC density in the
406 lesion core with progressively lower densities of OPCs observed in lesion edge and PLWM
407 regions respectively (Two-way ANOVA, region; $F(2,56) = 7.15$, $p = 0.0017$) (**Fig. 7G**). The inverse
408 pattern of OPC and OL density suggests region specific regulation of differentiation. We
409 quantitatively examined the axonal density in lesion edge and core (**Supplemental Fig. 2H**). As
410 expected, the lesion edge had significantly higher axonal density than core and corresponded
411 with the inverse relationship of OPC and OL densities in these regions (Two-way ANOVA, region;
412 $F(1,30) = 21.0$, $p < 0.0001$).
413 As successful remyelination in animal models is correlated with excess production of
414 OPCs, we sought to determine why OPC density never exceeded that of NAWM in the lesion
415 edge. Transient upregulation of $Sox2^+$ by activated OPCs is required for remyelination (Zhao et
416 al., 2015). We examined the proportion of $Sox2^+$ activated $Olig2^+$ cells in each region following
417 demyelination (**Fig. 7C**). We observed the greatest proportion of $Sox2^+$ OPCs in the lesion core
418 (Two-way ANOVA, region; $F(2,51) = 4.22$, $p = 0.02$) (**Fig. 7H**). The proportion of $Sox2^+$ OPCs
419 among $Olig2^+$ cells peaked at 14 dpl and declined thereafter. The relatively slow onset of Sox2
420 expression among rabbit OPCs suggested that other mechanisms may prevent OPC activation
421 and proliferation at earlier time points.

Pathological OPC quiescence may contribute to failed differentiation in the lesion edge.

We have previously shown that human OPCs overexpressing the transcription factor Prrx1 enter a reversible state of quiescence that prevents their cell-cycle entry and limits their capacity to myelinate host shiverer axons (Wang et al., 2018). Similar to previous reports, following induction of demyelination Prrx1 expression was found in both Olig2$^+$ oligodendrocyte lineage and other Olig2$^-$ cells (**Fig. 7I-J**). We noted a striking accumulation of Prrx1 expressing Olig2$^+$ cells in the lesion edge at 14 dpl (**Fig. 7I**). This was a transient phenomenon as the density and percentage of Prrx1$^+$Olig2$^+$ cells decreased significantly by 56 dpl (**Fig. 7J-L**). The accumulation of Prrx1$^+$Olig2$^+$ cells at the lesion edge suggests that OPCs entering the demyelinated region rapidly upregulated Prrx1 and likely become quiescent, thereby reducing their capacity to sufficiently repopulate the lesion. Consistent with altered OPC signaling in the rabbit, we observed occasional cytoplasmic Olig2 staining in the majority of sections analyzed with cells specifically localized around the edge of the lesion (**Fig. 7M**). The appearance of cytoplasmic Olig2 has been previously attributed to cells transitioning to an astroglial fate via IFN-γ (Cassiani-Ingoni et al., 2006).

Small volume lesions exhibited similar astrogliosis but relatively reduced microglial/macrophage responsiveness.

We next asked whether the deficits in OPC proliferation and differentiation could be attributed to lesion volume alone. We created small volume lesions via injection of 0.35 μL lysolecithin. Small volume lesions were 7-fold smaller by volume than large volume rabbit lesions, and closely resembled the volume of murine lesions (Kucharova et al., 2011) (murine lesions = 0.4 mm^3, small volume rabbit = 0.39 $\pm$ 0.1 mm^3, large volume rabbit = 3.6 $\pm$ 0.3 mm^3) (n=4 and 8, respectively) (**Fig. 8A-F, 8G**). Similar to large rabbit lesions, small volume lesions displayed equivalent levels of hypercellularity and astrogliosis (Gfap) compared to large volume lesions (**Fig. 8A-B, 8D-E**). Indeed, there were no significant differences between small and large volume lesions at any time point in terms of DAPI or GFAP (**Fig. 8H-I**). Intriguingly, we noted that small volume lesions had less intense Iba1 staining compared to large lesions (**Fig. 8C, 8F**) (Two-way ANOVA, volume: $F(1,28) = 17.39$, $p = 0.0003$). Mean Iba1 intensity was significantly decreased relative to large volume lesions at both 7 and 14 dpl (Sidak $p = 0.0015$ and 0.013, respectively) (**Fig. 8J**). Unlike larger volume lesions (1 and 5 μl), we did not observe a central region of axonal loss following injection of 0.35 μl lysolecithin (**Supplemental Fig. 2**). Axonal loss in small lesions was equivalent to that of the large lesion edge (**Supplemental Fig. 2I**).

453 **OPC activation and proliferation was substantially reduced in small rabbit lesions.**
454 To determine whether OPC repopulation was altered in small volume lesions, we interrogated
455 activation and proliferation of OPCs using Sox2 and Ki67, respectively (**Fig. 9**). We compared the
456 density of cells within the small lesion to the lesion edge of large volume lesions to exclude any
457 effects of the central region of axonal loss. The overall density of Olig2$^+$ cells following
458 demyelination was similar between large and small lesions (Two-way ANOVA, volume;
459 $F(1,22)=3.73$, $p > 0.05$) (**Fig. 9A, 9E**). However, unlike other animal models of spontaneous
460 remyelination, Olig2 density within the demyelinated lesion never exceeded that of normal
461 uninjured white matter regardless of lesion volume (dotted line).
462 Examination of Sox2 and Ki67 revealed far more apparent volume-dependent effects (**Fig.**
463 **9B-C**). The density of Sox2$^+$Olig2$^+$ cells was significantly lower in small vs. large lesions following
464 demyelination (Two-way ANOVA, volume; $F(1,21) = 24.38$, $p < 0.0001$). At 14 dpl, the extent of
465 Sox2 activation was >2-fold decreased in small lesions (Sidak's $p = 0.0003$) (**Fig. 9F**). This
466 corresponded with a profound reduction in the proportion of actively proliferating Ki67$^+$ OPCs
467 across time points (Two-way ANOVA, volume; $F(1,21) = 20.05$, $p = 0.0002$) (**Fig. 9G**). As Olig2
468 expression is maintained in OLs, we next examined the fraction of Ki67$^+$ cells among Sox2$^+$Olig2$^+$
469 activated OPCs (**Fig. 9H**). Very few, <1%, of these OPCs expressed Ki67 suggesting that OPC
470 proliferation is highly dependent on lesion volume in the rabbit and suggests that OPC
471 repopulation in small rabbit lesions is principally due to migration from NAWM.
472 Although proliferation was substantially lower in small volume lesions, there was
473 surprisingly no significant difference in the density of CC1$^-$Olig2$^+$ OPCs between small and large
474 volume lesions (Two-way ANOVA, volume; $F(1,22) = 0.25$, $p > 0.05$) (**Fig. 9I**). Large lesions with
475 7-fold greater volume requires approximately 2-3 more cell divisions to achieve the same density
476 of OPCs. The generation of CC1$^+$ OLs was not significantly different between small lesions and
477 the edge of large lesions (CC1$^+$Olig2$^+$ cell density; Two-way ANOVA, volume; $F(1,22) = 3.45$, $p >$
478 0.05) (**Fig. 9D, 9J**). Likewise, the rate of OL generation was equivalent between small and large
479 lesions (Two-way ANOVA, volume; $F(1,22) = 1.81$, $p > 0.05$) (**Fig. 9K**). These results suggest
480 that OPC activation and proliferation is highly influenced by lesion volume in the rabbit. Together,
481 these contribute to a failure to coordinate OPC recruitment with differentiation and together lead
482 to chronic demyelination.

DISCUSSION

Unlike murine models, spontaneous remyelination is inefficient in rabbit models with chronic demyelination persisting at least 6 months following injection of lysolecithin (Blakemore, 1978, Foster et al., 1980), and following induction of experimental autoimmune encephalomyelitis (EAE) (Williams et al., 1982, Prineas et al., 1969). Although reported over 40 years ago, the mechanisms underlying the failure of rabbit remyelination have not been investigated. Here, we show that the OPC response to demyelination is fundamentally altered in the rabbit brain relative to typically employed rodent models. In most rodent models, OPC density far exceeds that of normal white matter during the recruitment phase of remyelination. In contrast, rabbit OPC density slowly recovers following demyelination but never exceeds that observed in normal white matter. Deficient OPC proliferation and subsequently poor OPC repopulation in large rabbit lesions was associated with an upregulation of quiescence-associated genes and this corresponded with delayed and insufficient oligodendrocyte (OL) generation. In contrast, small rabbit lesions were essentially devoid of dividing OPCs and did not efficiently upregulate Sox2 in response to demyelination. As OPC repopulation was reduced in rabbit small lesions compared to mouse lesions of equivalent size, our results also highlight the potential importance of species-dependent differences in the response to demyelination (Dietz et al., 2016).

Parenchymal adult OPCs retain the capacity to generate new OLs and are largely considered to be the primary source of newly generated OLs following demyelination in the adult CNS (Serwanski et al., 2018, Zawadzka et al., 2010). In mouse models of toxin-induced demyelination and EAE, the OPC recruitment phase of remyelination is not typically rate limiting (Franklin and Goldman, 2015). Furthermore, approaches to improve OPC recruitment have not meaningfully altered the rate of myelin regeneration in focal mouse lesions. For example, overexpression of PDGF-AA drives enhanced OPC recruitment following demyelination and yet this had no discernable effect on the rate of remyelination (Woodruff et al., 2004). The progenitor pool in small rodent models is especially capable of efficient recruitment and occurs following systemic depletion either by X-irradiation (Chari and Blakemore, 2002) or pharmacogenetic depletion (Xing et al., 2021) and, importantly, after demyelination. Repeated focal demyelination is not sufficient to deplete the progenitor pool (Penderis et al., 2003) and only sustained depletion of OL lineage cells using 12-week treatment can prevent efficient remyelination in the cuprizone model (Mason et al., 2004). The relative success of OPC recruitment in the mouse is exemplified by the rapid regeneration of OPCs following demyelination, with a 2-3 fold increase in density over normal white matter (Sim et al., 2002, Ulrich et al., 2008, Kucharova and Stallcup, 2015, Lin et al., 2006). In contrast, rabbit lesions regardless of size are characterized by a failure of OPC

517 repopulation such that the density of OPCs never exceeds that of normal tissue and the
518 characteristic over-population of OPCs that occurs in the mouse and rat is absent. The rate of
519 OPC repopulation is also comparatively delayed, reaching peak density only after 14 days.
520 Whereas mouse and rats reach peak progenitor density within the first week (Sim et al., 2002,
521 Fancy et al., 2004). While the dynamics of OPC recruitment in humans is difficult to ascertain
522 from postmortem tissue, MS lesions rarely display OPC densities that exceed that of NAWM
523 (Lucchinetti et al., 1999, Kuhlmann et al., 2008, Boyd et al., 2013, Moll et al., 2013, Tepavcevic
524 et al., 2014). Demyelination of the optic nerve in non-human primates similarly lacks the abundant
525 recruitment of OPCs that is observed in murine models, with densities of OPCs and OLs not
526 recovering until 9 months after injection of lysolecithin (Sarrazin et al., 2022). Fascinatingly, even
527 at 9 months when OLs and OPC densities have recovered, few axons show evidence of
528 remyelination (Sarrazin et al., 2022). Together these data suggest that OPC recruitment in the
529 rabbit model more closely resembles that observed in MS and non-human primates.
530 While our data identify a substantial deficit in the ability of rabbit OPCs to repopulate
531 regions of demyelination, we also noted a relative failure in the ability of OPCs to undergo
532 differentiation. We observed a substantial decrease in the proportion of $CC1^+$ OLs among the
533 entire $Olig2^+$ lineage relative to mouse/rat model systems. In the lesion core, we observed fewer
534 OLs compared to other regions, and this corresponded with increased expression of markers of
535 tissue injury (including OPC, microglial, and astrocytic activation and axonal loss). Together, this
536 suggests the presence of a proinflammatory environment in the lesion core that contribute to failed
537 OL differentiation. An alternative hypothesis is that the failure of recruitment itself contributes to
538 failed differentiation. *In vitro* OL differentiation is dependent on the density of OPCs (Rosenberg
539 et al., 2008) and, similarly, following transplantation human OL differentiation is correlated with
540 the local density of human OPCs (Dietz et al., 2016). This suggests that below a certain threshold
541 local density of OPCs, the process of OL differentiation itself may be limited. Consistent with this
542 hypothesis, remyelinated lesions and active lesions in MS, which have a higher propensity for
543 remyelination, tend to have higher densities of OPCs than chronic demyelinated lesions (Boyd et
544 al., 2013). Lastly, at least within the central region of axonal loss, the failure of OL differentiation
545 may be due to the absence of an appropriate axonal substrate. This might also account for the
546 low density of OLs and relatively high density of OPCs found in the lesion core of large rabbit
547 lesions. Likewise, lysolecithin-induced lesions of non-human primate optic nerve induced
548 widespread axonal loss similar to the central region of axonal loss in the rabbit and display
549 similarly low densities of OLs (Sarrazin et al., 2022). However, axonal loss is unlikely to explain
550 the reduced density of OLs observed in edge of large rabbit lesions or across small volume lesions

551 where axonal loss is not as apparent. Chronic demyelination is observed following injection of 2.5
552 – 5 μL lysolecithin into the rabbit spinal cord at 6 months (Blakemore, 1978). While this is likely
553 recapitulated in this study (brain, 5 μL), it is possible that remyelination is more efficient in small
554 (0.35 μL) lesions or those localized to the cerebral white matter. It is worth noting that the density
555 of OLs in small lesions was not significantly greater than the lesion edge of large lesions and
556 reduced myelin content assessed by fluoromyelin remained evident at 21 dpl suggesting a similar
557 outcome. However, future ultrastructural analyses will be needed to elucidate this.
558 Several pieces of evidence in the current study point toward the importance of species
559 differences in OPC recruitment. Contrary to our initial hypothesis, the recovery of OPC density in
560 small volume lesions (0.4 mm^3) was not improved relative to large volume (4.0 mm^3) lesions and
561 the peak density of OPCs was unaffected by lesion volume. This suggests that lesion volume is
562 not the principal determinant of OPC recruitment. In contrast, OPC autonomous differences were
563 apparent between the rabbit and mouse. Sox2 is upregulated by OPCs following demyelination
564 in the mouse brain and is necessary for precursor proliferation (Zhao et al., 2015). On the other
565 hand, downregulation of Sox2 is required for subsequent differentiation. In murine models, Sox2
566 is rapidly upregulated in the majority of OPCs within a week of lesion formation. In contrast, OPCs
567 in the rabbit are slow to upregulate Sox2, failing to peak for at least 14 days. Sox2 expression
568 persists for several weeks in the rabbit but is not associated with continued OPC proliferation
569 suggesting a pathologic state of OPC activation. Furthermore, the transcriptional regulator Prrx1,
570 a transcription factor associated with OPC quiescence (Wang et al., 2018), was specifically
571 upregulated in numerous rabbit OPCs located at the lesion border. Prrx1 induces a reversible
572 state of quiescence inhibiting proliferation and thereby preventing efficient myelination (Wang et
573 al., 2018). Prrx1 itself is regulated by both interferon-γ and BMP signaling (Wang et al., 2018,
574 Saraswat et al., 2021b) and increased Prrx1 expression in the rabbit suggests that the lesion
575 environment may differ substantially from the mouse brain. Intriguingly, we also observed
576 prominent examples of cells expressing cytoplasmic Olig2 expression in the rabbit lesion that is
577 associated with an astroglial switch in stem/progenitor cells (Setoguchi, 2004) and observed in
578 rare cells in EAE (Cassiani-Ingoni et al., 2006). This is not observed in mouse lysolecithin lesions
579 and further supports species-specific differences in signaling. OPC autonomous differences
580 between species have been suggested by several other studies. For example, adult mouse OPCs
581 are more than twice as migratory compared to adult human OPCs (Bribian et al., 2020). Following
582 transplantation, human OPCs take 8-12 weeks to generate myelin-forming OLs (Sim et al., 2011,
583 Windrem et al., 2004, Windrem et al., 2008, Buchet et al., 2011), while equivalent rodent cells
584 typically complete the process of differentiation in 3-4 weeks (Baron-Van Evercooren and

585 Blakemore, 2004). Lastly, when human OPCs are transplanted into mouse brain, the human cells
586 outcompete their mouse counterparts suggestive of substantial differences in cell biology and
587 signaling between species (Windrem et al., 2014). Together, these results support the hypothesis
588 that species differences are critical determinants of the OPC response to demyelination.

589 Our analysis of small and large rabbit lesions revealed interesting differences in the
590 progenitor response to demyelination. The edge of large lesions and small lesions demonstrated
591 similar densities of OPC and OLs at every timepoint studied. Unlike large lesions, Ki67^{+} OPCs
592 were rarely observed in small lesions suggesting that the rate of proliferation was substantially
593 less and strongly influenced by the amount of tissue injury. In the current study, we could not
594 directly measure the contribution of migration to the general failure of OPC recruitment. However,
595 as we observed a similar density of cells in small and large lesions but with the absence of
596 proliferation in small lesions, this implies that OPC repopulation in small lesions may have been
597 largely dependent on migration from surrounding tissue rather than local expansion. This
598 corresponded with a much lower level of Sox2-expression amongst OPCs in small lesions and
599 suggests an altered transcriptional state dependent on lesion volume. In addition to volume-
600 dependent differences in the progenitor response, we also observed differences within individual
601 lesion such that significantly higher densities of OPCs were observed in the lesion core.
602 Proliferating Sox2^{+}Olig2^{+} cells were also largely found in the lesion core and this corresponded
603 with enhanced Iba1 and Gfap staining suggesting that the gliotic core was in part driving the
604 sustained OPC proliferation observed in that region. In contrast, we found increased generation
605 of OLs at the lesion border, a pattern commonly found in MS (Hess et al., 2020). The potential
606 mediators of these differences are outside the scope of the current study but further support the
607 importance of the local environment in the determination of OPC state and its capacity for both
608 proliferation and differentiation.

609 In summary, the rabbit model provides evidence for both species and volume dependent
610 effects on the cellular mechanisms of remyelination. Unlike mouse/rat models in which OPC and
611 oligodendrocyte densities far exceed normal white matter densities following demyelination, in the
612 rabbit these cells repopulate the lesion at a slower rate and never reach supernumerary densities.
613 When comparing mouse and rabbit lesions of equivalent size, we found that activation of Sox2
614 occurs more slowly, and that proliferation is almost absent in the rabbit. These processes are
615 themselves volume dependent as prolonged OPC proliferation and activation occurs in large
616 volume rabbit lesions. The failure of OPC proliferation, and subsequently OPC recruitment, in the
617 rabbit recapitulates the extent of OPC recruitment commonly observed in the majority of MS
618 lesions, as well as non-human primates, and thereby provides a suitable test bed for therapeutic

approaches aimed at improving the migration and proliferation of OPCs. As such, we propose that the simplicity and accessibility of the rabbit model along with the clear differences in lesion environment and patterns of OPC recruitment and differentiation will provide a vital complementary approach for preclinical testing of remyelination therapeutics and aid in the successful development of clinical interventions aimed at promoting myelin regeneration.

Conflict of Interest: The authors declare no competing financial interests.

Author Contributions:

Conception and design of the study: FJS and JJMC. Acquisition and analysis of data: all authors. Drafting the manuscript or figures: FJS and JJMC. Study supervision: FJS.

629 **REFERENCES**

630 ABSINTA, M., MARIC, D., GHARAGOZLOO, M., GARTON, T., SMITH, M. D., JIN, J.,
631 FITZGERALD, K. C., SONG, A., LIU, P., LIN, J. P., WU, T., JOHNSON, K. R.,
632 MCGAVERN, D. B., SCHAFER, D. P., CALABRESI, P. A. & REICH, D. S. 2021. A
633 lymphocyte-microglia-astrocyte axis in chronic active multiple sclerosis. *Nature,* 597**,** 709-
634 714.

635 BACMEISTER, C. M., BARR, H. J., MCCLAIN, C. R., THORNTON, M. A., NETTLES, D., WELLE,
636 C. G. & HUGHES, E. G. 2020. Motor learning promotes remyelination via new and
637 surviving oligodendrocytes. *Nat Neurosci,* 23**,** 819-831.

638 BARON-VAN EVERCOOREN, A. & BLAKEMORE, W. F. 2004. Chapter 6 - Remyelination
639 through Engraftment. *In:* LAZZARINI, R. A., GRIFFIN, J. W., LASSMAN, H., NAVE, K.-A.,
640 MILLER, R. & TRAPP, B. D. (eds.) *Myelin Biology and Disorders.* San Diego: Academic
641 Press.

642 BLAKEMORE, W. F. 1978. Observations on remyelination in the rabbit spinal cord following
643 demyelination induced by lysolecithin. *Neuropathol Appl Neurobiol,* 4**,** 47-59.

644 BOYD, A., ZHANG, H. & WILLIAMS, A. 2013. Insufficient OPC migration into demyelinated
645 lesions is a cause of poor remyelination in MS and mouse models. *Acta Neuropathol,* 125**,**
646 841-59.

647 BRIBIAN, A., MEDINA-RODRIGUEZ, E. M., JOSA-PRADO, F., GARCIA-ALVAREZ, I., MACHIN-
648 DIAZ, I., ESTEBAN, P. F., MURCIA-BELMONTE, V., VEGA-ZELAYA, L., PASTOR, J.,
649 GARRIDO, L. & DE CASTRO, F. 2020. Functional Heterogeneity of Mouse and Human
650 Brain OPCs: Relevance for Preclinical Studies in Multiple Sclerosis. *J Clin Med,* 9.

651 BROWN, J. W. L., CUNNIFFE, N. G., PRADOS, F., KANBER, B., JONES, J. L., NEEDHAM, E.,
652 GEORGIEVA, Z., ROG, D., PEARSON, O. R., OVERELL, J., MACMANUS, D., SAMSON,
653 R. S., STUTTERS, J., FFRENCH-CONSTANT, C., GANDINI WHEELER-KINGSHOTT,
654 C. A. M., MORAN, C., FLYNN, P. D., MICHELL, A. W., FRANKLIN, R. J. M., CHANDRAN,
655 S., ALTMANN, D. R., CHARD, D. T., CONNICK, P. & COLES, A. J. 2021. Safety and
656 efficacy of bexarotene in patients with relapsing-remitting multiple sclerosis (CCMR One):
657 a randomised, double-blind, placebo-controlled, parallel-group, phase 2a study. *The*
658 *Lancet Neurology,* 20**,** 709-720.

659 BUCHET, D., GARCIA, C., DEBOUX, C., NAIT-OUMESMAR, B. & BARON-VAN
660 EVERCOOREN, A. 2011. Human neural progenitors from different foetal forebrain regions
661 remyelinate the adult mouse spinal cord. *Brain,* 134**,** 1168-83.

662 CADAVID, D., MELLION, M., HUPPERTS, R., EDWARDS, K. R., CALABRESI, P. A.,
663 DRULOVIĆ, J., GIOVANNONI, G., HARTUNG, H.-P., ARNOLD, D. L., FISHER, E.,
664 RUDICK, R., MI, S., CHAI, Y., LI, J., ZHANG, Y., CHENG, W., XU, L., ZHU, B., GREEN,
665 S. M., CHANG, I., DEYKIN, A., SHEIKH, S. I., AGÜERA MORALES, E., AL KHEDR, A.,
666 AMPAPA, R., ARROYO, R., BELKIN, M., BONEK, R., BOYKO, A., CAPRA, R.,
667 CENTONZE, D., CLAVELOU, P., DEBOUVERIE, M., DRULOVIC, J., EDWARDS, K.,
668 EVANGELOU, N., EVDOSHENKO, E., FERNÁNDEZ, O., FERNÁNDEZ SÁNCHEZ, V.,
669 FREEDMAN, M., FREEDMAN, S., FRYZE, W., GARCIA-MERINO, A., GAVRIC-KEZIC,
670 M., GHEZZI, A., GOUT, O., GRIMALDI, L., HENDIN, B., HERTMANOWSKA, H.,
671 HINTZEN, R., HRADILEK, P., HUPPERTS, R., ILKOWSKI, J., IVASHINENKOVA, E.,
672 IZQUIERDO, G., JACQUES, F., JAKAB, G., KHABIROV, F., KLODOWSKA-DUDA, G.,
673 KOMOLY, S., KOSTIC, S., KOVAROVA, I., KREMENCHUZKY, M., LAGANKE, C.,
674 LAPIERRE, Y., MACIEJOWSKI, M., MAISON, F. G., MARFIA, G. A., MARTÍNEZ
675 YÉLAMOS, S., MELUZINOVA, E., MONTALBAN, X., MURRAY, R., NAISMITH, R.,
676 NEWSOME, S., NGUYEN, V., OREJA, D., PARDO, G., PASECHNIK, E., PATTI, F.,
677 POTEMKOWSKI, A., PROKOPENKO, S., QIAN, P., RODRÍGUEZ-ANTIGÜEDAD, A.,
678 ROSSMAN, H., ROZSA, C., SÁNCHEZ LÓPEZ, F., SELMAJ, K., SILBER, E., STEPIEN,
679 A., STEPNIEWSKA, A., SWIAT, M., TONCEV, G., TOURBAH, A., TRUSHNIKOVA, T.,
680 UCCELLI, A., VACHOVA, M., VALIS, M., VECSEI, L., WIERTLEWSKI, S., ZAFFARONI,
681 M., et al. 2019. Safety and efficacy of opicinumab in patients with relapsing multiple
682 sclerosis (SYNERGY): a randomised, placebo-controlled, phase 2 trial. *The Lancet*
683 *Neurology,* 18**,** 845-856.

684 CASSIANI-INGONI, R., COKSAYGAN, T., XUE, H., REICHERT-SCRIVNER, S. A., WIENDL, H.,
685 RAO, M. S. & MAGNUS, T. 2006. Cytoplasmic translocation of Olig2 in adult glial
686 progenitors marks the generation of reactive astrocytes following autoimmune
687 inflammation. *Exp Neurol,* 201**,** 349-58.

688 CHARI, D. M. & BLAKEMORE, W. F. 2002. Efficient recolonisation of progenitor-depleted areas
689 of the CNS by adult oligodendrocyte progenitor cells. *Glia,* 37**,** 307-13.

690 DIETZ, K. C., POLANCO, J. J., POL, S. U. & SIM, F. J. 2016. Targeting human oligodendrocyte
691 progenitors for myelin repair. *Exp Neurol,* 283**,** 489-500.

692 DUNCAN, I. D., RADCLIFF, A. B., HEIDARI, M., KIDD, G., AUGUST, B. K. & WIERENGA, L. A.
693 2018. The adult oligodendrocyte can participate in remyelination. *Proc Natl Acad Sci U S*
694 *A,* 115**,** E11807-E11816.

695 FANCY, S. P., BARANZINI, S. E., ZHAO, C., YUK, D. I., IRVINE, K. A., KAING, S., SANAI, N.,
696 FRANKLIN, R. J. & ROWITCH, D. H. 2009. Dysregulation of the Wnt pathway inhibits
697 timely myelination and remyelination in the mammalian CNS. *Genes Dev,* 23**,** 1571-85.
698 FANCY, S. P., ZHAO, C. & FRANKLIN, R. J. 2004. Increased expression of Nkx2.2 and Olig2
699 identifies reactive oligodendrocyte progenitor cells responding to demyelination in the
700 adult CNS. *Mol Cell Neurosci,* 27**,** 247-54.
701 FOSTER, R. E., KOCSIS, J. D., MALENKA, R. C. & WAXMAN, S. G. 1980. Lysophosphatidyl
702 choline-induced focal demyelination in the rabbit corpus callosum. Electron-microscopic
703 observations. *J Neurol Sci,* 48**,** 221-31.
704 FRANKLIN, R. J. & GOLDMAN, S. A. 2015. Glia Disease and Repair-Remyelination. *Cold Spring*
705 *Harb Perspect Biol,* 7**,** a020594.
706 FRANKLIN, R. J. M. & FFRENCH-CONSTANT, C. 2017. Regenerating CNS myelin - from
707 mechanisms to experimental medicines. *Nat Rev Neurosci,* 18**,** 753-769.
708 GARAY, L., TUNGLER, V., DENISELLE, M. C., LIMA, A., ROIG, P. & DE NICOLA, A. F. 2011.
709 Progesterone attenuates demyelination and microglial reaction in the lysolecithin-injured
710 spinal cord. *Neuroscience,* 192**,** 588-97.
711 GREEN, A. J., GELFAND, J. M., CREE, B. A., BEVAN, C., BOSCARDIN, W. J., MEI, F., INMAN,
712 J., ARNOW, S., DEVEREUX, M., ABOUNASR, A., NOBUTA, H., ZHU, A., FRIESSEN,
713 M., GERONA, R., VON BÜDINGEN, H. C., HENRY, R. G., HAUSER, S. L. & CHAN, J. R.
714 2017. Clemastine fumarate as a remyelinating therapy for multiple sclerosis (ReBUILD):
715 a randomised, controlled, double-blind, crossover trial. *The Lancet,* 390**,** 2481-2489.
716 HESS, K., STAROST, L., KIERAN, N. W., THOMAS, C., VINCENTEN, M. C. J., ANTEL, J.,
717 MARTINO, G., HUITINGA, I., HEALY, L. & KUHLMANN, T. 2020. Lesion stage-dependent
718 causes for impaired remyelination in MS. *Acta Neuropathol,* 140**,** 359-375.
719 HUANG, J. K., JARJOUR, A. A., FFRENCH-CONSTANT, C. & FRANKLIN, R. J. 2011. Retinoid
720 X receptors as a potential avenue for regenerative medicine in multiple sclerosis. *Expert*
721 *Rev Neurother,* 11**,** 467-8.
722 HUGHES, E. G., KANG, S. H., FUKAYA, M. & BERGLES, D. E. 2013. Oligodendrocyte
723 progenitors balance growth with self-repulsion to achieve homeostasis in the adult brain.
724 *Nat Neurosci,* 16**,** 668-76.
725 JEAN, I., LAVIALLE, C., BARTHELAIX-POUPLARD, A. & FRESSINAUD, C. 2003. Neurotrophin-
726 3 specifically increases mature oligodendrocyte population and enhances remyelination
727 after chemical demyelination of adult rat CNS. *Brain Res,* 972**,** 110-8.

728 KOHLER, C., WAHL, H., ZIEMSSEN, T., LINN, J. & KITZLER, H. H. 2019. Exploring individual
729 multiple sclerosis lesion volume change over time: Development of an algorithm for the
730 analyses of longitudinal quantitative MRI measures. *Neuroimage Clin,* 21**,** 101623.
731 KOTTER, M. R., LI, W. W., ZHAO, C. & FRANKLIN, R. J. 2006. Myelin impairs CNS remyelination
732 by inhibiting oligodendrocyte precursor cell differentiation. *J Neurosci,* 26**,** 328-32.
733 KUCHAROVA, K., CHANG, Y., BOOR, A., YONG, V. W. & STALLCUP, W. B. 2011. Reduced
734 inflammation accompanies diminished myelin damage and repair in the NG2 null mouse
735 spinal cord. *J Neuroinflammation,* 8**,** 158.
736 KUCHAROVA, K. & STALLCUP, W. B. 2015. NG2-proteoglycan-dependent contributions of
737 oligodendrocyte progenitors and myeloid cells to myelin damage and repair. *J*
738 *Neuroinflammation,* 12**,** 161.
739 KUHLMANN, T., MIRON, V., CUI, Q., WEGNER, C., ANTEL, J. & BRUCK, W. 2008.
740 Differentiation block of oligodendroglial progenitor cells as a cause for remyelination failure
741 in chronic multiple sclerosis. *Brain,* 131**,** 1749-58.
742 LIN, W., KEMPER, A., DUPREE, J. L., HARDING, H. P., RON, D. & POPKO, B. 2006. Interferon-
743 gamma inhibits central nervous system remyelination through a process modulated by
744 endoplasmic reticulum stress. *Brain,* 129**,** 1306-18.
745 LUBETZKI, C., SOL-FOULON, N. & DESMAZIERES, A. 2020. Nodes of Ranvier during
746 development and repair in the CNS. *Nat Rev Neurol,* 16**,** 426-439.
747 LUCCHINETTI, C., BRUCK, W., PARISI, J., SCHEITHAUER, B., RODRIGUEZ, M. &
748 LASSMANN, H. 1999. A quantitative analysis of oligodendrocytes in multiple sclerosis
749 lesions. A study of 113 cases. *Brain,* 122 (Pt 12)**,** 2279-95.
750 MASON, J. L., TOEWS, A., HOSTETTLER, J. D., MORELL, P., SUZUKI, K., GOLDMAN, J. E. &
751 MATSUSHIMA, G. K. 2004. Oligodendrocytes and progenitors become progressively
752 depleted within chronically demyelinated lesions. *Am J Pathol,* 164**,** 1673-82.
753 MCGINLEY, M. P., GOLDSCHMIDT, C. H. & RAE-GRANT, A. D. 2021. Diagnosis and Treatment
754 of Multiple Sclerosis: A Review. *JAMA,* 325**,** 765-779.
755 MEI, F., FANCY, S. P. J., SHEN, Y. A., NIU, J., ZHAO, C., PRESLEY, B., MIAO, E., LEE, S.,
756 MAYORAL, S. R., REDMOND, S. A., ETXEBERRIA, A., XIAO, L., FRANKLIN, R. J. M.,
757 GREEN, A., HAUSER, S. L. & CHAN, J. R. 2014. Micropillar arrays as a high-throughput
758 screening platform for therapeutics in multiple sclerosis. *Nat Med,* 20**,** 954-960.
759 MELLION, M., EDWARDS, K. R., HUPPERTS, R., DRULOVIC, J., MONTALBAN, X., HARTUNG,
760 H. P., BROCHET, B., CALABRESI, P. A., RUDICK, R., IBRAHIM, A., ZHANG, Y. W., XU,
761 L. & CADAVID, D. 2017. Efficacy Results from the Phase 2b SYNERGY Study: Treatment

762 of Disabling Multiple Sclerosis with the Anti-LINGO-1 Monoclonal Antibody Opicinumab.
763 *Neurology,* 88.
764 MI, S., MILLER, R. H., LEE, X., SCOTT, M. L., SHULAG-MORSKAYA, S., SHAO, Z., CHANG,
765 J., THILL, G., LEVESQUE, M., ZHANG, M., HESSION, C., SAH, D., TRAPP, B., HE, Z.,
766 JUNG, V., MCCOY, J. M. & PEPINSKY, R. B. 2005. LINGO-1 negatively regulates
767 myelination by oligodendrocytes. *Nat Neurosci,* 8**,** 745-51.
768 MOLL, N. M., HONG, E., FAUVEAU, M., NARUSE, M., KERNINON, C., TEPAVCEVIC, V.,
769 KLOPSTEIN, A., SEILHEAN, D., CHEW, L. J., GALLO, V. & OUMESMAR, B. N. 2013.
770 SOX17 is expressed in regenerating oligodendrocytes in experimental models of
771 demyelination and in multiple sclerosis. *Glia*.
772 NEUMANN, B., BAROR, R., ZHAO, C., SEGEL, M., DIETMANN, S., RAWJI, K. S., FOERSTER,
773 S., MCCLAIN, C. R., CHALUT, K., VAN WIJNGAARDEN, P. & FRANKLIN, R. J. M. 2019.
774 Metformin Restores CNS Remyelination Capacity by Rejuvenating Aged Stem Cells. *Cell*
775 *Stem Cell,* 25**,** 473-485 e8.
776 PENDERIS, J., SHIELDS, S. A. & FRANKLIN, R. J. 2003. Impaired remyelination and depletion
777 of oligodendrocyte progenitors does not occur following repeated episodes of focal
778 demyelination in the rat central nervous system. *Brain,* 126**,** 1382-91.
779 PRINEAS, J., RAINE, C. S. & WÍSNIEWSKI, H. 1969. An ultrastructural study of experimental
780 demyelination and remyelination. 3. Chronic experimental allergic encephalomyelitis in the
781 central nervous system. *Lab Invest,* 21**,** 472-83.
782 ROSEN, G. D. & HARRY, J. D. 1990. Brain volume estimation from serial section measurements:
783 a comparison of methodologies. *J Neurosci Methods,* 35**,** 115-24.
784 ROSENBERG, S. S., KELLAND, E. E., TOKAR, E., DE LA TORRE, A. R. & CHAN, J. R. 2008.
785 The geometric and spatial constraints of the microenvironment induce oligodendrocyte
786 differentiation. *Proc Natl Acad Sci U S A,* 105**,** 14662-7.
787 RUSIELEWICZ, T., NAM, J., DAMANAKIS, E., JOHN, G. R., RAINE, C. S. & MELENDEZ-
788 VASQUEZ, C. V. 2014. Accelerated repair of demyelinated CNS lesions in the absence
789 of non-muscle myosin IIB. *Glia,* 62**,** 580-91.
790 SARASWAT, D., SHAYYA, H. J., POLANCO, J. J., TRIPATHI, A., WELLIVER, R. R., POL, S. U.,
791 SEIDMAN, R. A., BROOME, J. E., O'BARA, M. A., VAN KUPPERVELT, T. H., PHILLIPS,
792 J. J., DUTTA, R. & SIM, F. J. 2021a. Overcoming the inhibitory microenvironment
793 surrounding oligodendrocyte progenitor cells following experimental demyelination. *Nat*
794 *Commun,* 12**,** 1923.

795 SARASWAT, D., WELLIVER, R. R., RAVICHANDAR, R., TRIPATHI, A., POLANCO, J. J.,
796 BROOME, J., HURLEY, E., DUTTA, R., FELTRI, M. L. & SIM, F. J. 2021b. Heparanome-
797 Mediated Rescue of Oligodendrocyte Progenitor Quiescence following Inflammatory
798 Demyelination. *J Neurosci,* 41**,** 2245-2263.
799 SARRAZIN, N., CHAVRET-RECULON, E., BACHELIN, C., FELFLI, M., ARAB, R., GILARDEAU,
800 S., BRAZHNIKOVA, E., DUBUS, E., YAHA-CHERIF, L., LORENCEAU, J., PICAUD, S.,
801 ROSOLEN, S., MOISSONNIER, P., POUGET, P. & BARON-VAN EVERCOOREN, A.
802 2022. Failed remyelination of the nonhuman primate optic nerve leads to axon
803 degeneration, retinal damages, and visual dysfunction. *Proc Natl Acad Sci U S A,* 119**,**
804 e2115973119.
805 SERWANSKI, D. R., RASMUSSEN, A. L., BRUNQUELL, C. B., PERKINS, S. S. & NISHIYAMA,
806 A. 2018. Sequential Contribution of Parenchymal and Neural Stem Cell-Derived
807 Oligodendrocyte Precursor Cells toward Remyelination. *Neuroglia,* 1**,** 91-105.
808 SETOGUCHI, T. 2004. Nuclear export of OLIG2 in neural stem cells is essential for ciliary
809 neurotrophic factor-induced astrocyte differentiation. *The Journal of Cell Biology,* 166**,**
810 963-968.
811 SIM, F. J., MCCLAIN, C. R., SCHANZ, S. J., PROTACK, T. L., WINDREM, M. S. & GOLDMAN,
812 S. A. 2011. CD140a identifies a population of highly myelinogenic, migration-competent
813 and efficiently engrafting human oligodendrocyte progenitor cells. *Nat Biotechnol,* 29**,** 934-
814 41.
815 SIM, F. J., ZHAO, C., PENDERIS, J. & FRANKLIN, R. J. 2002. The age-related decrease in CNS
816 remyelination efficiency is attributable to an impairment of both oligodendrocyte progenitor
817 recruitment and differentiation. *J Neurosci,* 22**,** 2451-9.
818 TEPAVCEVIC, V., KERNINON, C., AIGROT, M. S., MEPPIEL, E., MOZAFARI, S., ARNOULD-
819 LAURENT, R., RAVASSARD, P., KENNEDY, T. E., NAIT-OUMESMAR, B. & LUBETZKI,
820 C. 2014. Early netrin-1 expression impairs central nervous system remyelination. *Ann*
821 *Neurol,* 76**,** 252-68.
822 ULRICH, R., SEELIGER, F., KREUTZER, M., GERMANN, P. G. & BAUMGARTNER, W. 2008.
823 Limited remyelination in Theiler's murine encephalomyelitis due to insufficient
824 oligodendroglial differentiation of nerve/glial antigen 2 (NG2)-positive putative
825 oligodendroglial progenitor cells. *Neuropathol Appl Neurobiol,* 34**,** 603-20.
826 WANG, J., SARASWAT, D., SINHA, A. K., POLANCO, J., DIETZ, K., O'BARA, M. A., POL, S. U.,
827 SHAYYA, H. J. & SIM, F. J. 2018. Paired Related Homeobox Protein 1 Regulates
828 Quiescence in Human Oligodendrocyte Progenitors. *Cell Rep,* 25**,** 3435-3450 e6.

829 WAXMAN, S. G., KOCSIS, J. D. & NITTA, K. C. 1979. Lysophosphatidyl choline-induced focal
830 demyelination in the rabbit corpus callosum. Light-microscopic observations. *J Neurol Sci,*
831 44**,** 45-53.
832 WILLIAMS, R. M., LEES, M. B., CAMBI, F. & MACKLIN, W. B. 1982. Chronic Experimental
833 Allergic Encephalomyelitis Induced in Rabbits with Bovine White Matter Proteolipid
834 Apoprotein. *Journal of Neuropathology & Experimental Neurology,* 41**,** 508-521.
835 WINDREM, M. S., NUNES, M. C., RASHBAUM, W. K., SCHWARTZ, T. H., GOODMAN, R. A.,
836 MCKHANN, G., 2ND, ROY, N. S. & GOLDMAN, S. A. 2004. Fetal and adult human
837 oligodendrocyte progenitor cell isolates myelinate the congenitally dysmyelinated brain.
838 *Nat Med,* 10**,** 93-7.
839 WINDREM, M. S., SCHANZ, S. J., GUO, M., TIAN, G. F., WASHCO, V., STANWOOD, N.,
840 RASBAND, M., ROY, N. S., NEDERGAARD, M., HAVTON, L. A., WANG, S. &
841 GOLDMAN, S. A. 2008. Neonatal chimerization with human glial progenitor cells can both
842 remyelinate and rescue the otherwise lethally hypomyelinated shiverer mouse. *Cell Stem*
843 *Cell,* 2**,** 553-65.
844 WINDREM, M. S., SCHANZ, S. J., MORROW, C., MUNIR, J., CHANDLER-MILITELLO, D.,
845 WANG, S. & GOLDMAN, S. A. 2014. A competitive advantage by neonatally engrafted
846 human glial progenitors yields mice whose brains are chimeric for human glia. *J Neurosci,*
847 34**,** 16153-61.
848 WOLSWIJK, G. 1998. Chronic stage multiple sclerosis lesions contain a relatively quiescent
849 population of oligodendrocyte precursor cells. *J Neurosci,* 18**,** 601-9.
850 WOODRUFF, R. H., FRUTTIGER, M., RICHARDSON, W. D. & FRANKLIN, R. J. 2004. Platelet-
851 derived growth factor regulates oligodendrocyte progenitor numbers in adult CNS and
852 their response following CNS demyelination. *Mol Cell Neurosci,* 25**,** 252-62.
853 XING, Y. L., CHUANG, B. H. A., POH, J., MORADI, K., MITEW, S., KILPATRICK, T. J., OSANAI,
854 Y. & MERSON, T. D. 2021. A Novel Pharmacogenetic Model for Highly Efficient Ablation
855 of Oligodendrocyte Progenitor Cells in the Adult Mouse CNS. *bioRxiv***,**
856 2021.05.13.443012.
857 YEUNG, M. S. Y., DJELLOUL, M., STEINER, E., BERNARD, S., SALEHPOUR, M., POSSNERT,
858 G., BRUNDIN, L. & FRISEN, J. 2019. Publisher Correction: Dynamics of oligodendrocyte
859 generation in multiple sclerosis. *Nature,* 566**,** E9.
860 ZAWADZKA, M., RIVERS, L. E., FANCY, S. P., ZHAO, C., TRIPATHI, R., JAMEN, F., YOUNG,
861 K., GONCHAREVICH, A., POHL, H., RIZZI, M., ROWITCH, D. H., KESSARIS, N.,
862 SUTER, U., RICHARDSON, W. D. & FRANKLIN, R. J. 2010. CNS-resident glial

863 progenitor/stem cells produce Schwann cells as well as oligodendrocytes during repair of
864 CNS demyelination. *Cell Stem Cell,* 6**,** 578-90.
865 ZHAO, C., MA, D., ZAWADZKA, M., FANCY, S. P., ELIS-WILLIAMS, L., BOUVIER, G.,
866 STOCKLEY, J. H., DE CASTRO, G. M., WANG, B., JACOBS, S., CASACCIA, P. &
867 FRANKLIN, R. J. 2015. Sox2 Sustains Recruitment of Oligodendrocyte Progenitor Cells
868 following CNS Demyelination and Primes Them for Differentiation during Remyelination.
869 *J Neurosci,* 35**,** 11482-99.

870

871

872 **TABLES**

Table 1. Animal and lesion numbers per timepoint.

Timepoint (dpl)	Large Lesions		Small Lesions	
	Animals	Lesions	Animals	Lesions
7	6	9	4	6
14	5	8	4	4
21	4	8	4	4
56	5	7		
180	3	4		

873

874 **FIGURE LEGENDS**

875 **Figure 1. Large regions of demyelination following injection of lysolecithin into rabbit**
876 **subcortical white matter persisted for at least 180 days. A**, Scale diagram representing
877 injection sites and white matter tract size (mouse included for reference). **B**, Lysolecithin-induced
878 lesion at 14 days post-lesion (dpl) in the rabbit stained for FluoroMyelin (FM, red) and 4',6'-
879 diamidino-2-phenylindole (DAPI, blue). White dotted line indicates lesion border. **C-D**, Lesion
880 volume (**C**) and maximal cross-sectional area (**D**) of lesions overtime. **E**, lesion reconstruction
881 using FM and DAPI sampled every 1.6 mm, demonstrating typical lesion geometry at 7 dpl. Each
882 point represents a single lesion. Mean ± SEM shown. Scale: 5 mm (**A**), 500 μm (**B**), 300 μm (**E**).

883

884 **Figure 2. Insufficient oligodendrocyte progenitor cell repopulation and oligodendrocyte**
885 **generation following demyelination in rabbit white matter. A**, Oligodendrocyte progenitor
886 cells (OPCs) and oligodendrocytes (OLs) were identified as $Olig2^{+}CC1^{-}$ and $Olig2^{+}CC1^{+}$,
887 respectively. Insert shows a high magnification image of a $CC1^{+}$ (green) OL. The density of each
888 cell type was quantified at each time point (**B-E**). **B**, Density of $Olig2^{+}$ oligodendrocyte lineage
889 cells. **C**, Density of $CC1^{-}Olig2^{+}$ defined OPCs cells. **D,** Density of $CC1^{+}Olig2^{+}$ defined OLs. **E**, The
890 percentage of $CC1^{+}$ oligodendrocytes among total $Olig2^{+}$ OL lineage cells. Mean ± SEM shown.
891 Dashed line on each graph represents the mean of normal white matter (left bar, n = 6). Following
892 one-way ANOVA, pairwise comparisons to normal were performed (Tukey's multiple comparisons
893 post-test). *, **, ***, and **** indicate $p \leq 0.05$, 0.01, 0.001, and 0.0001, respectively. Scale: 50 μm
894 (**A**), 10 μm (**A**, insert).

895

896 **Figure 3. Abundant oligodendrocyte progenitor cell activation but low proliferation**
897 **following injury. A-D**, Representative images of normal white matter (**A**), or lesion at 14 days
898 post-lesion (dpl) (**B**), 56 dpl (**C**), 180 dpl (**D**). Activated Sox2$^+$ OPCs (cyan), proliferative Ki67$^+$
899 OPCs (green) were identified by colocalization with Olig2 (red). Insert shows high magnification
900 of labelled cells. Individual Sox2$^+$Olig2$^+$ cells are indicated with arrows in **C** and **D**. **E**, Density of
901 activated Sox2$^+$ OPCs following demyelination. **F**, Proportion of Ki67$^+$ proliferating Olig2$^+$ cells. **G**,
902 Proportion of Ki67$^+$ proliferating cells among Sox2$^+$Olig2$^+$ activated OPCs. **H**, An example of Sox2
903 (cyan)-expressing Gfap$^+$ (green) astrocyte within the demyelinating lesion. **I**, Quantification of
904 Sox2$^+$Olig2$^-$ astrocytic cell density. Mean ± SEM shown. Dashed lines on graph represent mean
905 of normal white matter (left bar, n =6). One-way ANOVA was performed across time points and
906 specific pairwise comparisons are shown, between normal and peak, peak and 180 dpl, and
907 normal and 180 dpl (other pairwise comparisons excluded for clarity) (Tukey's multiple
908 comparisons post-test). *, **, ***, and **** indicate $p \leq 0.05$, 0.01, 0.001, and 0.0001, respectively.
909 Scale: 200 µm (**A-D**), 10 µm (**A**, inserts), 5 µm (**H**).
910
911 **Figure 4. Large lesions displayed abundant gliosis, with the microglia/macrophage**
912 **response greatest at early timepoints. A-D**, Iba1 (red) and Gfap (green) were used as markers
913 of microglia/macrophages and astrocytes, respectively, with nuclei labeled with DAPI (blue).
914 Lesion borders (dashed line). Inserts show higher power confocal images of boxed areas. **E**, Iba1
915 mean fluorescent intensity (MFI). The intensity of staining in the distant corpus callosum was
916 considered normal appearing white matter (NAWM) for quantitative comparisons and to control
917 for batch and animal staining variability. **F**, Total Gfap$^+$ area above threshold was quantified and
918 shown as a percentage of total lesion area. **G**, DAPI$^+$ cell density within the lesion (cells / mm^2).
919 Mean ± SEM shown. Dashed lines on graph represent mean of distant normal appearing white
920 matter (NAWM) (n= 29) or normal uninjured animals (n=3). Following one-way ANOVA, pairwise
921 comparisons to NAWM were performed (Tukey's multiple comparisons post-test). *, **, ***, and
922 **** indicate $p \leq 0.05$, 0.01, 0.001, and 0.0001, respectively. Scale: 500 µm (**A-D**), 25 µm (**A**,
923 inserts).
924
925 **Figure 5. Myelin ladened microglia/macrophages were abundant within the lesion center**
926 **of large rabbit lesions. A-B**, Low power imaging revealed Iba1$^+$ (red) vesicular structures filling
927 the lesion core at 14 (**A**) and 56 dpl (**B**). **C-E**, Confocal microscopy with DAPI (blue)(**C**), myelin
928 basic protein (Mbp, gray) (**D**, same field), and neurofilament (NF, green) (**E**) co-staining with Iba1
929 (red). The majority of vesicular structures surrounded by Iba1$^+$ immunoreactivity contained myelin

930 debris at 14 dpl while a small minority contained neurofilament. At 56 dpl, a substantial proportion
931 of vesicular structures did not contain immunoreactivity to Mbp or NF. Scale: 100 μm (**A-B**), 20
932 μm (**C-E**).
933
934 **Figure 6. The perilesion white matter displayed hypercellularity and disturbed myelin**
935 **structure. A**, Evolution of lysolecithin-induced lesions in the rabbit over time stained for
936 FluoroMyelin (FM, red) and DAPI (blue/cyan). White dashed line indicates lesion bounds. An area
937 of hypercellularity extending past the lesion boundary was noted (blue dashed line), referred to
938 as the perilesion white matter (PLWM). **A'**, Higher magnification images of the outlined areas
939 (white rectangles) depicting the observed cellularity changes between lesion, PLWM, and more
940 distant normal appearing white matter (NAWM). **B**, Quantification of observed changes in
941 cellularity between the different regions at 21 dpl (n = 6-22, one-way ANOVA, $F(3,38) = 147.3$, p
942 $= 0.0001$). Mean ± SEM shown. Dashed lines on graph represent mean of normal white matter.
943 Following one-way ANOVA, pairwise comparisons to NAWM were performed (Tukey's multiple
944 comparisons post-test). *, **, ***, and **** indicate $p \leq 0.05$, 0.01, 0.001, and 0.0001, respectively.
945 **C**, Comparison of mean maximal cross-sectional area of lesion and PLWM areas. **D-E**,
946 Representative confocal images of NAWM stained for myelin (Mbp, gray), and axonal markers
947 (NF, green; App, red). **F-G**, Following demyelination at 7 to 56 dpl, lesions were imaged by
948 widefield epifluorescence (left panels). **F'-G'**, Higher power confocal images within the lesion
949 (right panels). Myelin loss was evident in the lesion following injection of lysolecithin and persisted
950 thereafter. Myelin debris was present in the lesion core at all timepoints. Axonal loss was localized
951 to the central portion of the lesion and corresponded to increased App (red) staining at 7 dpl.
952 Scale: 500 μm (**A, F-G**), 100 μm (**A'**), 25 μm (**D-E, F'-G'**).
953
954 **Figure 7. Oligodendrocyte density was reduced in the perilesion white matter, with**
955 **increased expression of Prrx1 among OPCs at the lesion edge. A-E**, Three regions were
956 defined for regional analysis: perilesion white matter (PLWM) (light green dashed line), lesion
957 edge (green dashed line), and lesion core (dark green dashed line). PLWM was defined as an
958 area of mild hypercellularity and extended past the lesion border. The lesion proper was divided
959 into the edge and core regions, with the edge defined as the outermost 75μm rim. Cross-sectional
960 columns of a 56 dpl lesion covering the various regions stained for DAPI (**A**), OLs ($Olig2^+CC1^+$)
961 (**B**), active oligodendrocyte progenitor cell ($Olig2^+Sox2^+$) (**C**), proliferative OPCs ($Olig2^+Ki67^+$) (**D**),
962 and $Gfap^+$ astrocytes (**E**). **F-H**, Quantification of cell density and/or proportion of total
963 oligodendrocyte linage cells between regions for OLs ($Olig2^+CC1^+$, **F**), OPCs ($Olig2^+CC1^-$, **G**), and

964 activated OPCs (Olig2$^+$Sox2$^+$, **H**). Mean ± SEM shown. Horizontal bands represent mean ± 1x
965 SEM of the normal white matter for each measurement (n = 3 rabbits). Two-way ANOVA was
966 performed across time (TME: time main effect) and regions (RME: regional main effect). *, **, ***,
967 and **** indicate p ≤ 0.05, 0.01, 0.001, and 0.0001, respectively. Individual pairwise comparisons
968 not shown. **I-J**, a combination of *in situ* hybridization and immunohistochemistry was used to label
969 Prrx1 mRNA (gray) and Olig2 protein (red). Arrowheads indicate coexpression of Olig2 and Prrx1.
970 **K-L**, Density (**K**), and percentage (**L**) of Prrx1$^+$Olig2$^+$ cells in the lesion edge. Mean ± SEM shown
971 (n=3). * and *** indicate t-test p ≤ 0.05 and 0.001, respectively. **M**, an example of a cytoplasmic
972 Olig2 immunoreactive cell at 56 dpl. These cells were observed in most lesion sections following
973 demyelination (~1-2 cells per section, most commonly at 56 dpl). Scale: 200 μm (**A-E**), 10 μm
974 (**M**).
975
976 **Figure 8. Small rabbit lesions displayed a reduced microglial response.** Small (0.35 μL) (**A-**
977 **C**) and large (5 μL) (**D-F**) volume lesions were created via stereotaxic injection of lysolecithin, and
978 stained for DAPI (blue), Gfap (green), and Iba1(red). White dashed lines indicate lesion border.
979 **G**, Lesion volume calculated by serial section reconstruction of each lesion. **H**, Lesion cell density
980 (DAPI$^+$/mm^2). **I**, Quantification of astrocyte response. Total Gfap$^+$ area above threshold was
981 quantified and shown as a percentage of total lesion area. **J**, microglial response was quantified
982 by mean fluorescent intensity (MFI). Mean ± SEM shown. Dashed lines on graph represent mean
983 of distant normal appearing white matter (n= 29). 0.35 μL injections of lysolecithin produced
984 lesions with significantly smaller volumes as compared to 5 μL at every time point (n= 4-9, two-
985 way ANOVA, volume factor $F(1,33) = 72.5$, $p < 0.0001$). Small and large volume lesions displayed
986 similar levels of hypercellularity (volume factor $F(1,21) = 3.37$, $p > 0.05$), and similar astrocyte
987 responses (n= 4-9, two-way ANOVA, volume factor $F(1,32) = 0.05$, $p > 0.05$). However, Iba1 MFI
988 was significantly greater in large volume lesions compared to small lesions (n= 4-9, two-way
989 ANOVA, volume factor $F(1,28) = 17.39$, $p = 0.0003$). Pairwise comparisons of small vs. large
990 lesions at each time point shown for lesion volume (**G**) and microglial response (**J**) (Sidak's
991 multiple comparisons post-test). *, **, ***, and **** indicate p ≤ 0.05, 0.01, 0.001, and 0.0001,
992 respectively. Scale: 200 μm.
993
994 **Figure 9. Small volume lesions displayed less oligodendrocyte progenitor cell activation**
995 **and dramatically reduced proliferation. A-C**, Activated Sox2$^+$ oligodendrocyte progenitor cells
996 (OPCs) (**B**, cyan), and proliferative Ki67$^+$ OPCs (**C**, green) were identified by colocalization with
997 Olig2 at 14 dpl in small and large volume lesions. Insert shows higher magnification of labelled

998 cells. **D**, Oligodendrocyte (OL) differentiation was assessed by CC1 (green) and Olig2 (red)
999 immunofluorescence. A representative $CC1^+Olig2^+$ cell is shown (**D**, inset). In large lesions, the
1000 quantification of cell density was performed in the lesion edge. **E-K**, Quantification of $Olig2^+$ OL
1001 lineage cell density (cells/mm^2, **E**), the density of $Sox2^+Olig2^+$ activated OPCs (cell/mm^2, **F**), the
1002 percentage of Ki67-defined proliferating $Olig2^+$ cells (**G**), the percentage of Ki67-defined
1003 proliferating $Sox2^+Olig2^+$ OPCs (**H**), density of $CC1^-Olig2^+$ cells (cells/mm^2, **I**), density of
1004 $CC1^+Olig2^+$ oligodendrocytes (cells/mm^2, **J**), and the percentage of $CC1^+Olig2^+$ oligodendrocytes
1005 among the $Olig2^+$ population (**K**) in small and large lesions. Mean ± SEM shown. Dashed lines on
1006 each graph represent mean of normal uninjured white matter (n = 3 rabbits). **E-K**, Two-way
1007 ANOVA revealed a significant effects of lesion volume on activated (**F**) and proliferating (**G-H**)
1008 OPC densities ($p < 0.05$). The other endpoints were not significantly altered by lesion volume.
1009 **F-H**, Pairwise comparisons of small vs. large lesions at each time point were performed and
1010 shown where significant (Sidak multiple comparisons post-test). *, **, ***, and **** indicate $p \leq$
1011 0.05, 0.01, 0.001, and 0.0001, respectively. Scale: 50 µm (**A-D**), 10 µm (**B-D**, insets).
1012
1013 **Supplemental Figure 1. Markers of the innate immune response were increased in the**
1014 **perilesion white matter adjacent to demyelination.** The white matter directly adjacent to the
1015 lesion area, termed the perilesion white matter (PLWM), and defined by increased cellularity
1016 compared to normal white matter exhibited increased staining for markers of microglia and
1017 astrocytes following demyelination. White dashed line indicates lesion bounds, and the PLWM
1018 was identified as an area of DAPI hypercellularity (**A**, blue) extending past the lesion boundary
1019 (blue dashed line). Iba1 was used to identify microglia (**B**, red) and astrocytes identified using
1020 Gfap (**C**, green). **D-E,** Quantification of Iba1 mean fluorescence intensity (MFI) (**D**), and Gfap %
1021 area (**E**). Mean ± SEM shown. Dashed lines on each graph represent mean of normal appearing
1022 white matter (NAWM). One-way ANOVA revealed a significant effect of time on both Iba1 and
1023 Gfap. Pairwise comparisons to NAWM were performed at each dpl (Tukey's multiple comparisons
1024 post-test). *, and **** indicate $p \leq 0.05$, and 0.0001, respectively. Scale, 250 µm.
1025
1026 **Supplemental Figure 2. Axon deficient center was dependent on lysolecithin injection**
1027 **volume.** Axonal density following demyelination was assessed by neurofilament
1028 immunofluorescence (green) as a function of volume of lysolecithin injected and days post lesion
1029 (dpl). DAPI (blue) hypercellularity was used to define the lesion border (outer white line).
1030 Neurofilament-expressing axonal fibers were observed throughout the lesion following injection
1031 of 0.35 µL (**A**) at 7 days post-lesion (dpl). With injections of 1 µL (**B**) and 5 µL (**C**), a central region

1032 of axonal loss was observed at 7 dpl (orange lines). The area of central axonal loss increased
1033 with injection volume. **C-F**, the central area of axonal loss persisted until 56 dpl. The area of the
1034 central region of axonal loss (orange line) compared to the total lesion area (grey line) (**G**). The
1035 size of the central region of axonal loss remained stable with time, while the overall lesion area
1036 reduced. **H**, Axonal density in the lesion edge was compared to the lesion core (which contained
1037 the central region of axonal loss). Quantitative estimation of axonal density following 5 μL
1038 lysolecithin injection was performed using a thresholding approach. Mean ± SEM shown. Dashed
1039 lines on each graph represent mean of normal appearing white matter (NAWM). Two-way ANOVA
1040 showed a significantly greater axonal density in the lesion edge than core ($n = 8\text{-}14$, region main
1041 effect $p < 0.0001$) and indicated a time dependent effect on axonal density (time main effect $p =$
1042 0.014). Pairwise comparisons of 14, 21 and 56 dpl with 7 dpl identified a significant decrease in
1043 axonal density at 21 and 56 dpl in the lesion core only (* indicates Sidak $p \leq 0.05$). **I,** the axonal
1044 density in small lesions was directly compared to the axonal density in large lesion edge at 7 dpl.
1045 Mean ± SEM shown. There was no significant difference (t-test $p > 0.05$). Scale, 200 μm.
1046
1047 **Supplemental Figure 3. Summary of oligodendroglia population dynamics in small and**
1048 **large lesions, compared to mouse.** Meta-analysis of rabbit large and small lesions alongside
1049 equivalently sized mouse spinal cord lesions. Comparative mouse data obtained from previously
1050 published quantification of oligodendrocyte progenitor cell (OPC)/NG2 density (Garay et al., 2011,
1051 Kucharova and Stallcup, 2015), oligodendrocyte (OL)/Plp1 (Fancy et al., 2009), $Sox2^+Olig2^+$
1052 OPCs and $Ki67^+Olig2^+$ OPCs (Zhao et al., 2015 and unpublished data). **A**, Table summarizing
1053 the effects of species and lesion volume on various cellular parameters following demyelination.
1054 The time of peak density in days post lesion (dpl) as well as the density relative to normal
1055 uninjured white matter are presented for OPC repopulation, OL repopulation, activated OPC
1056 density ($Sox2^+$), and proliferating OPC density ($Ki67^+$). ↑ and ↑↑ indicate significant increases in
1057 density relative to uninjured normal white matter. ns = non-significant from normal white matter
1058 density. **B**, Scale diagrams comparing large and small rabbit lesions and mouse spinal cord
1059 lesions. **C**, Profiles of overall OPC density and the relative density of $Sox2^+$ activated and $Ki67^+$
1060 proliferating OPCs. Scale, 2 mm.

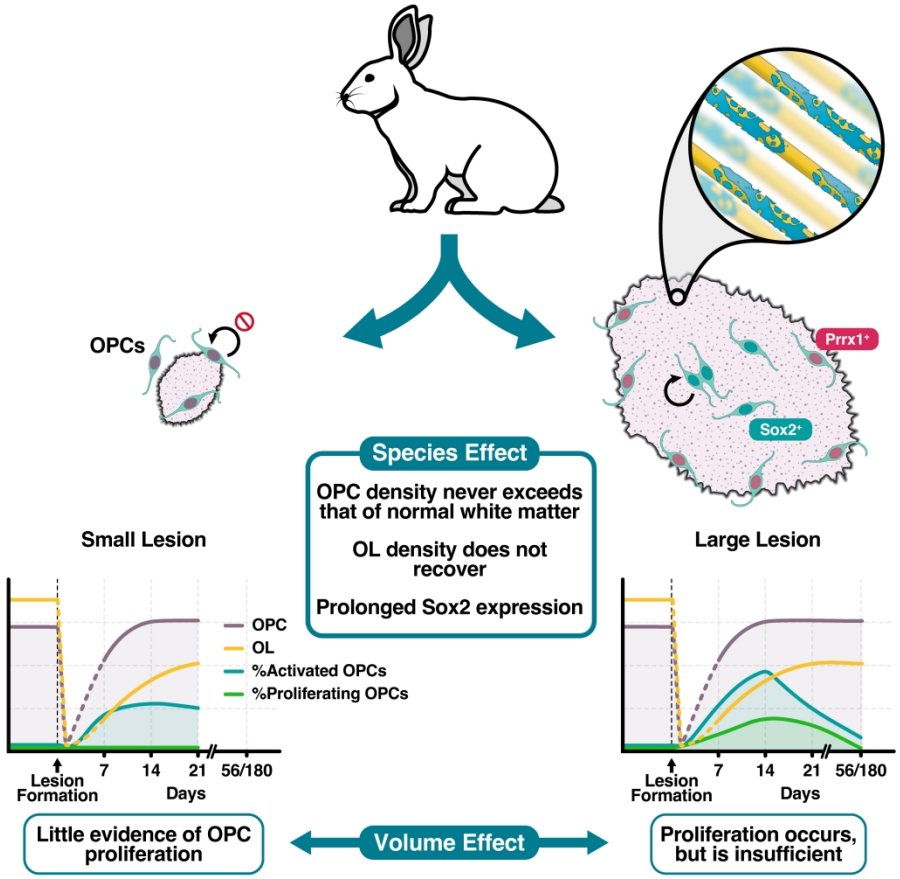

Graphical Abstract

287x257mm (300 x 300 DPI)

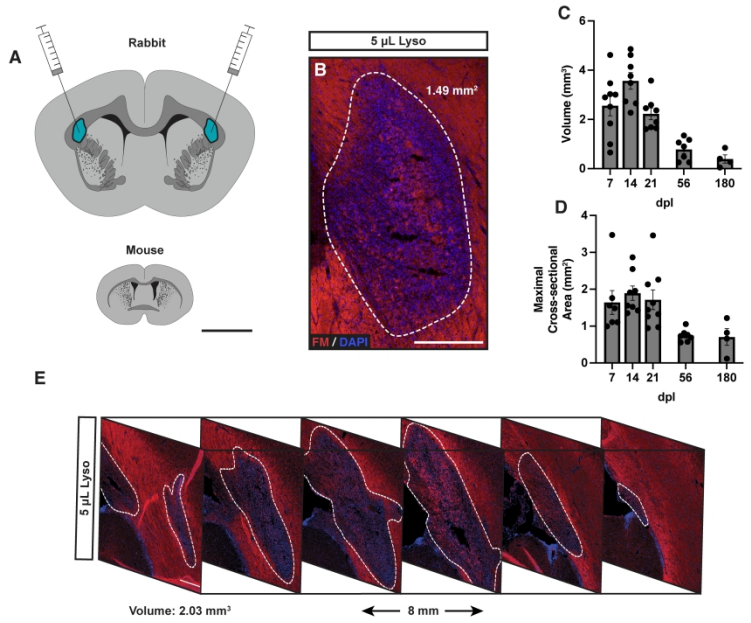

Figure 1. Large regions of demyelination following injection of lysolecithin into rabbit subcortical white matter persisted for at least 180 days.

416x263mm (300 x 300 DPI)

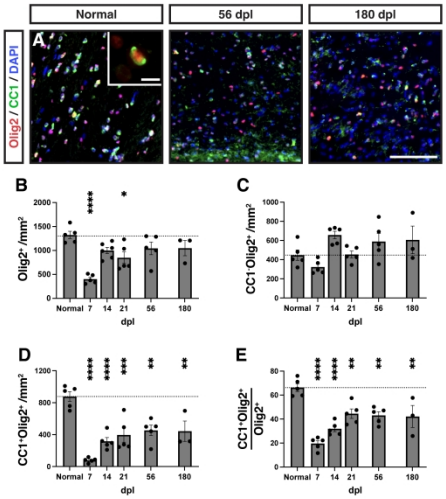

Figure 2. Insufficient oligodendrocyte progenitor cell repopulation and oligodendrocyte generation following demyelination in rabbit white matter

416x234mm (300 x 300 DPI)

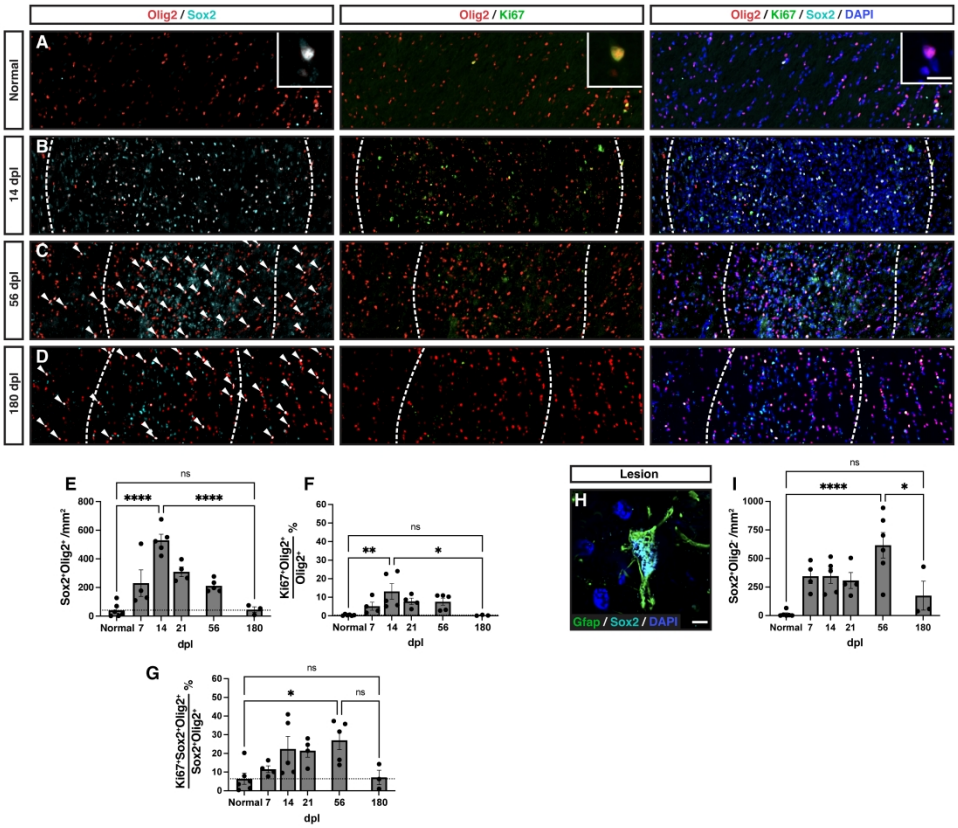

Figure 3. Abundant oligodendrocyte progenitor cell activation but low proliferation following injury.

416x365mm (300 x 300 DPI)

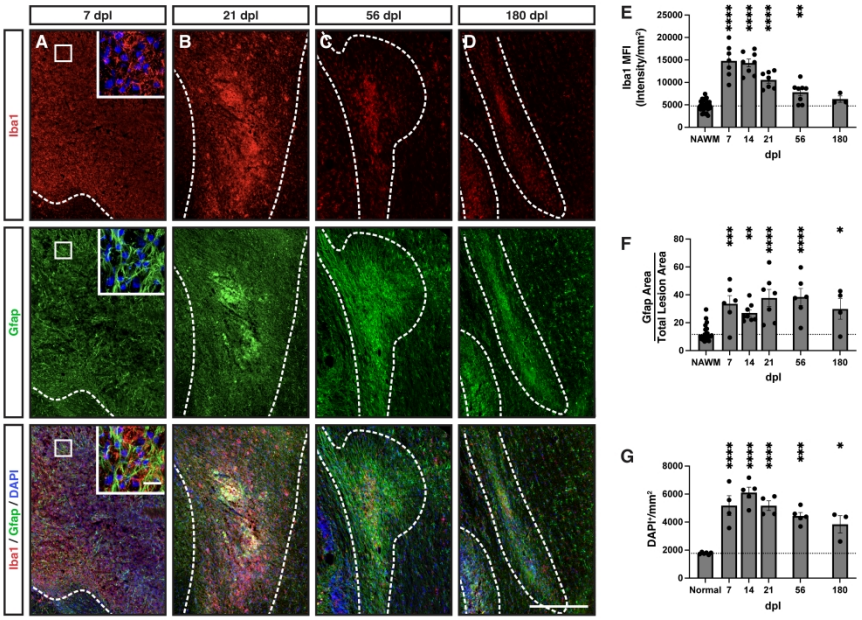

Figure 4. Large lesions displayed abundant gliosis, with the microglia/macrophage response greatest at early timepoints.

416x287mm (300 x 300 DPI)

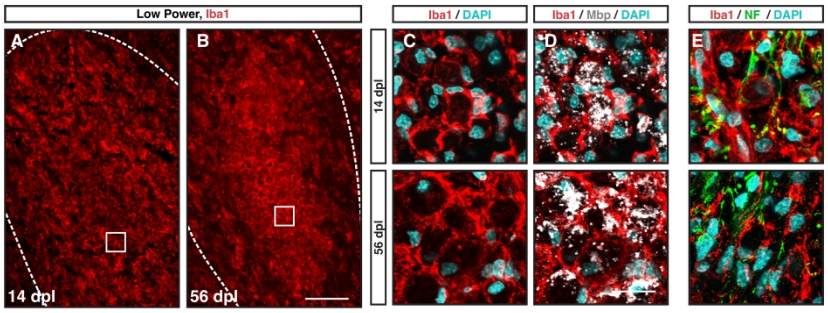

Figure 5. Myelin ladened microglia/macrophages were abundant within the lesion center of large rabbit lesions.

416x150mm (300 x 300 DPI)

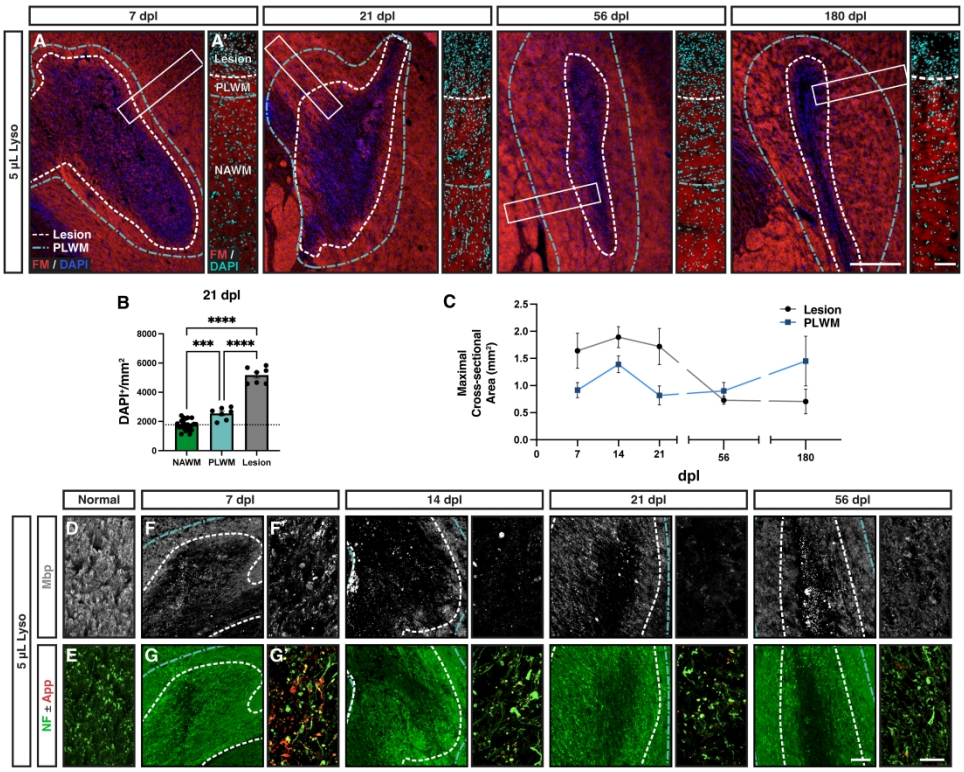

Figure 6. The perilesion white matter displayed hypercellularity and disturbed myelin structure.

416x347mm (300 x 300 DPI)

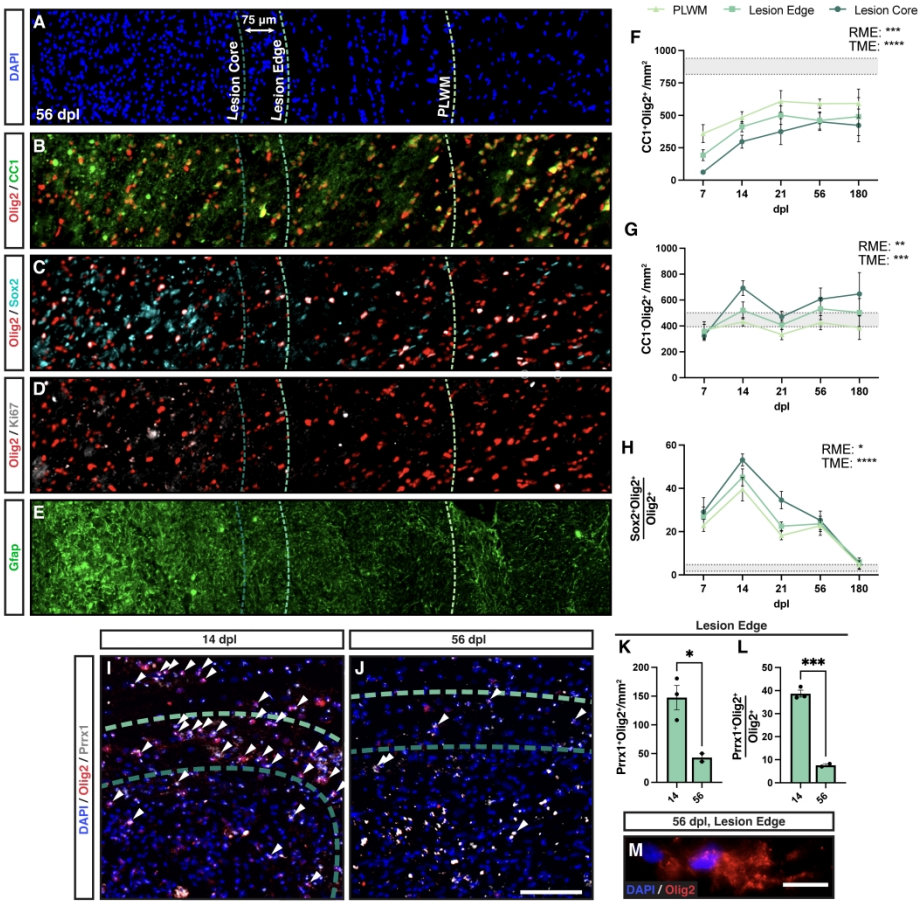

Figure 7. Oligodendrocyte density was reduced in the perilesion white matter, with increased expression of Prrx1 among OPCs at the lesion edge.

416x397mm (300 x 300 DPI)

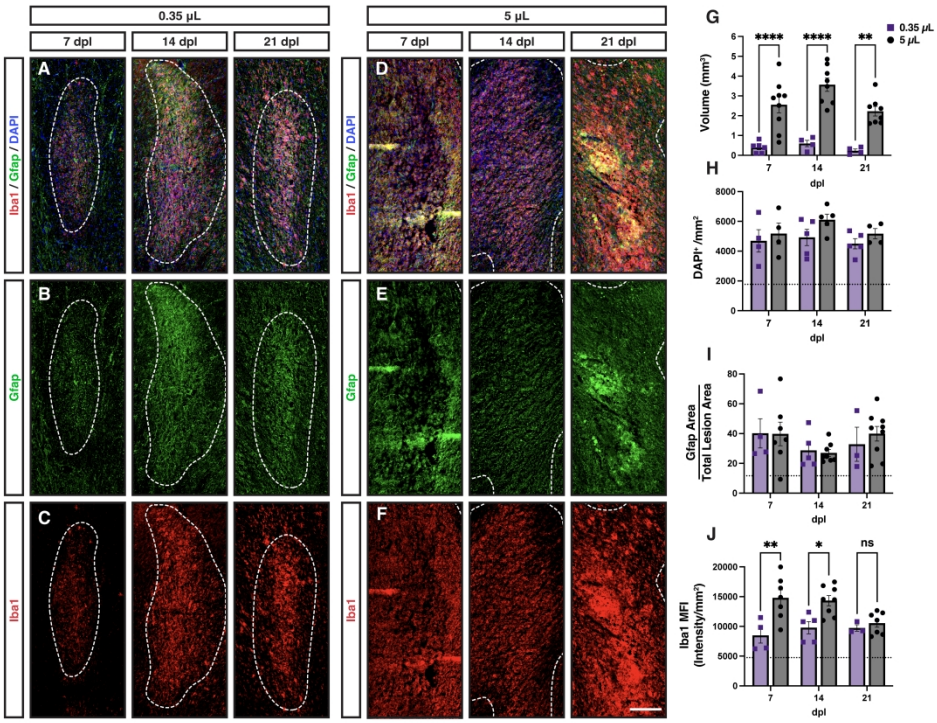

Figure 8. Small rabbit lesions displayed a reduced microglial response.

416x344mm (300 x 300 DPI)

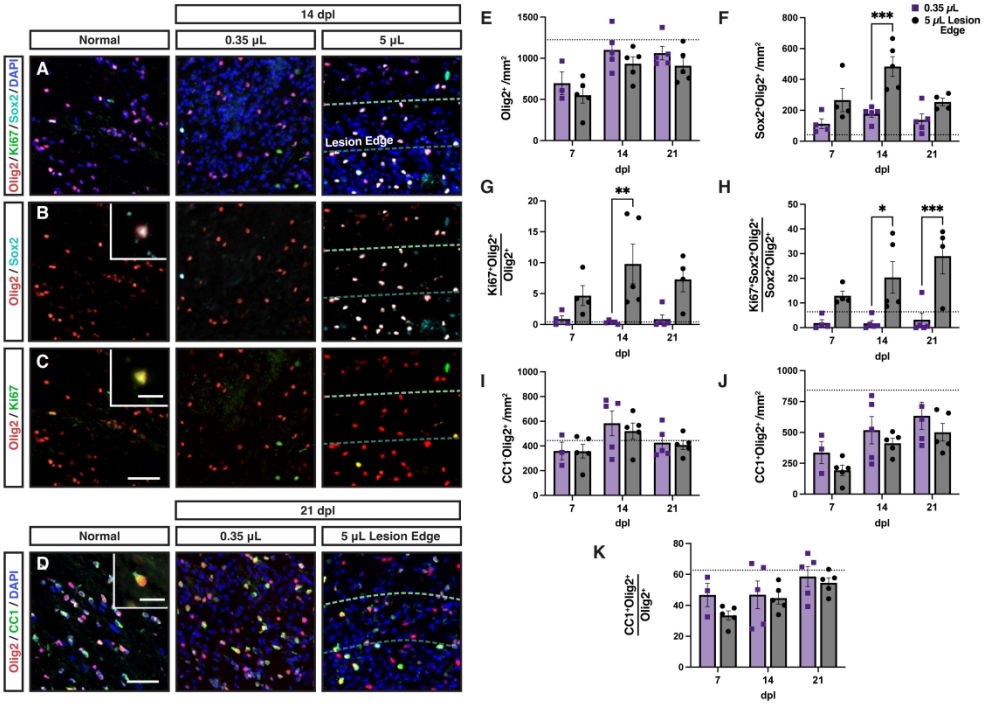

Figure 9. Small volume lesions displayed less oligodendrocyte progenitor cell activation and dramatically reduced proliferation.

416x312mm (300 x 300 DPI)

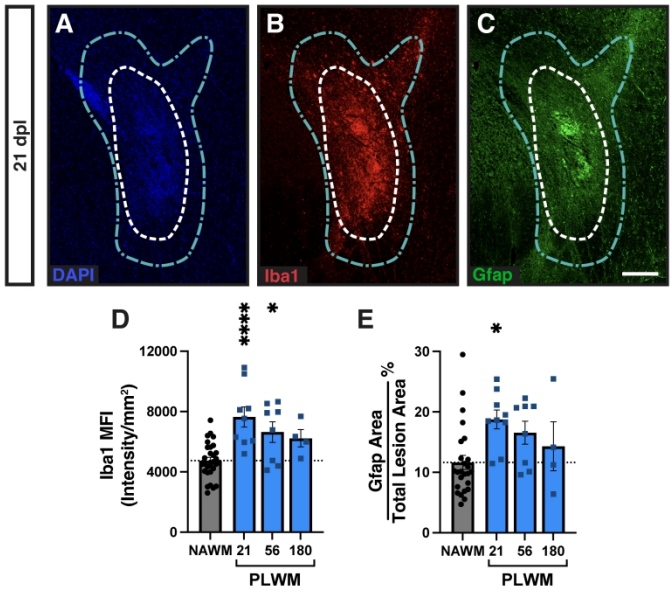

Supplemental Figure 1. Markers of the innate immune response were increased in the perilesion white matter adjacent to demyelination.

282x185mm (300 x 300 DPI)

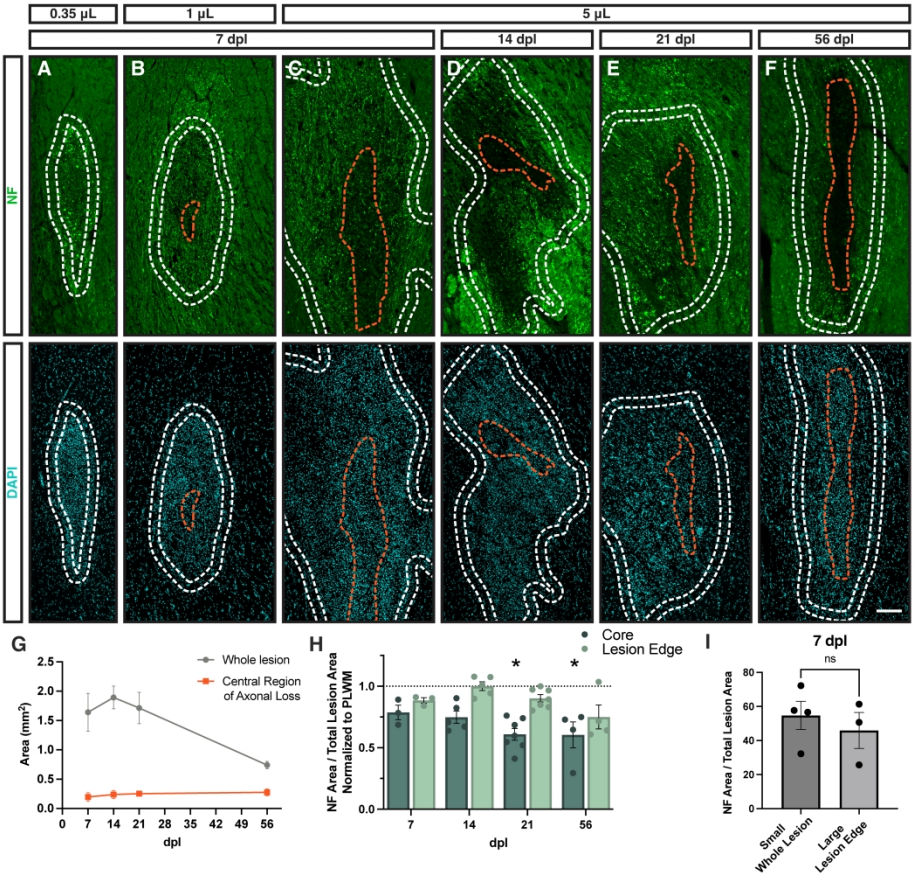

Supplemental Figure 2. Axon deficient center was dependent on lysolecithin injection volume.

367x355mm (300 x 300 DPI)

A

	Rabbit				Mouse	
	Large Lesion		Small Lesion		Spinal Cord	
Parameter	Peak	Values	Peak	Values	Peak	Values
OPC Repopulation	14 dpl	ns	14 dpl	ns	*7 dpl*	↑↑
OL Repopulation	21 dpl	ns	21 dpl	ns	*14 dpl*	↑↑
% Activated OPC ($Sox2^+Olig2^+$)	14 dpl	↑↑	14 dpl	↑	*5 dpl*	↑↑
% Proliferating OPC ($Ki67^+Olig2^+$)	14 dpl	↑	14 dpl	ns	*5 dpl*	↑

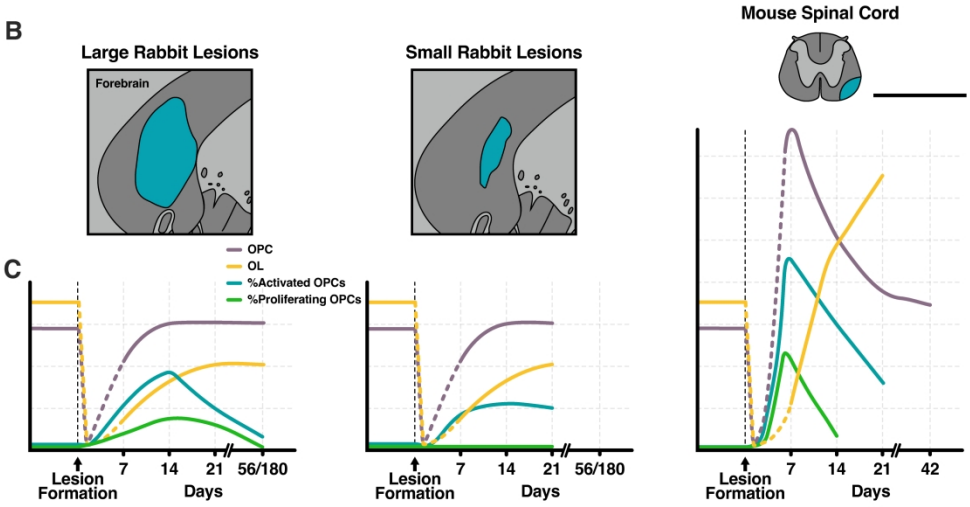

Supplemental Figure 3. Summary of oligodendroglia population dynamics in small and large lesions, compared to mouse.

294x230mm (300 x 300 DPI)